Strategies for Enhancing Electrochemical CO_2 Reduction to Multi-Carbon Fuels on Copper

Xin Li,[1,#] Yuxin Chen,[1,#] Xinyu Zhan,[1] Yiwen Xu,[1] Leiduan Hao,[1] Liang Xu,[1] Xueying Li,[1] Muhammad Umer,[1] Xinyi Tan,[2,*] Buxing Han,[3,*] Alex W. Robertson,[4] and Zhenyu Sun[1,*]

[1] State Key Laboratory of Organic-Inorganic Composites, College of Chemical Engineering, Beijing University of Chemical Technology, Beijing 100029, P. R. China.

Corresponding email: sunzy@mail.buct.edu.cn

[2] School of Materials Science and Engineering, Beijing Institute of Technology, Beijing Key Laboratory of Environmental Science and Engineering, Beijing 100081, P. R. China.

Corresponding email: xinyitan@bit.edu.cn

[3] Institute of Chemistry, Chinese Academy of Sciences, Beijing 100190, P. R. China.

Corresponding email: hanbx@iccas.ac.cn

[4] Department of Physics, University of Warwick, Coventry CV 47AL, UK.

[#] These authors contribute equally to this work.

Abstract

Productively harnessing CO_2 as a reactant is of practical interest due to it addressing the dual pressures of resource sustainability and environmental sustainability. Electrochemical CO_2 reduction (ECR) offers a promising approach for driving the chemical transformation of CO_2 by exploiting green renewably generated electricity at (near) room temperature and ambient pressure, facilitating a sustainable, low-carbon footprint future. In this work, we provide a comprehensive and timely review of the various avenues that have been developed to date to modulate product selectivity, stability, and efficiency toward C_{2+} using Cu-based electrocatalysts. We discuss how the electrocatalyst structure can be effectively designed in order to boost performance. Special attention is paid to some of the critical intermediate species that shed light on CO_2 reduction paths. We will also discuss the application of in situ and operando spectroscopy,

along with computational techniques, that help to improve our fundamental understanding of ECR. Finally, development opportunities and challenge in the conversion of CO_2 into multi-carbon fuels by Cu-based electrocatalysts are presented.

Keywords
CO_2 reduction; electrocatalysis; multi-carbon products; copper

1. Introduction

Anthropogenic carbon dioxide (CO_2) emissions from the use of fossil fuels have exacerbated the greenhouse effect from our planet's atmosphere, with the CO_2 concentration exceeding 421 ppm as of May 2022 (National Oceanic and Atmospheric Administration, Fig. 1), intensifying the pace of climate change [1, 2]. To combat this continued warming, extensive efforts are now required in the development of CO_2 sequestration and conversion technologies [3]. CO_2 is the most abundant carbon-based resource, and could thus be an ideal carbon source for a myriad of valuable products, such as feedstock chemicals, polymers, pharmaceuticals, and fuels [4, 5]. Transformation of CO_2 into useful products not only reduces CO_2 emissions, but also provides an alternative carbon source to polluting and finite fossil fuels [6, 7]. Thus productively harnessing CO_2 as a reactant has practical application in addressing both resource sustainability and environmental sustainability. In particular, electrochemical CO_2 reduction (ECR) (in the presence of water) offers a promising strategy for driving CO_2 chemical transformation by exploiting green renewable electricity from solar, wind, nuclear, tidal, marine, or geothermal sources under (or near) room temperature and ambient pressure (Fig. 2), enabling a sustainable and low-carbon footprint future [8]. A fully green process would also eliminate the use of fossil fuels as the H_2 source, with hydrogen instead being generated in situ by water electrolysis. Of particular interest is that this approach can integrate renewable electricity into transportation systems and into chemical manufacturing, due to it offering a path

for converting green energy into carbon containing products without the need for fossil fuels. Utilization of electrocatalysis provides further advantages due to decentralization, and would be of great value in supplementing the upcoming surplus of cheap electrical energy generated from intermittent and distributed renewable sources that would otherwise require costly energy storage technologies. An electrochemical reaction system offers a practical, compact, and on demand solution, thus would be of significant practical use.

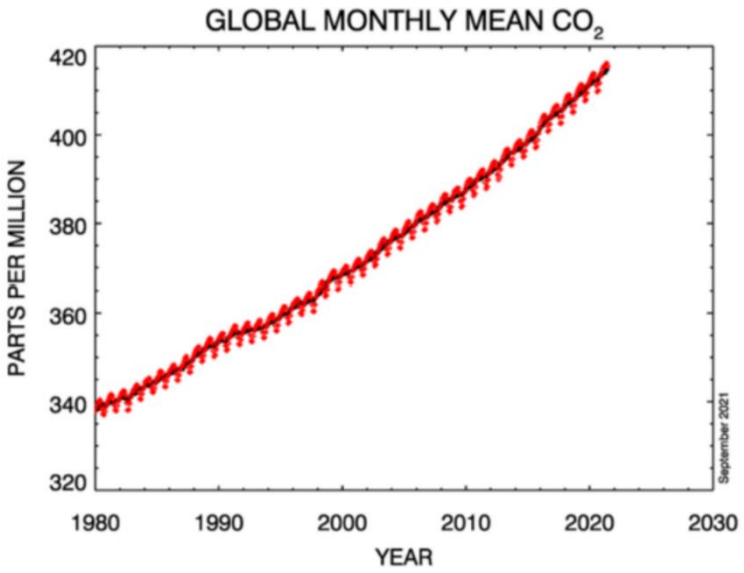

Figure 1. The global concentration of mid-tropospheric carbon dioxide in parts per million (ppm) as time goes on. The data are collected from https://gml.noaa.gov/ccgg/trends/global.html.

Research on ECR dates back to at least the 1950s [9]. Quantification of both the gaseous and liquid products was pioneered by Yoshio Hori and co-workers in the 1980s [10]. Publications peaked in the mid-1990s, then falling to a low in the 2000s with 10 to 20 papers per year. However, as the cost of renewable electricity decreased and more energy storage was required, a strong revival in interest in performing ECR studies arose in the early 2010s. Now, hundreds of papers are published every year on the subject of ECR.

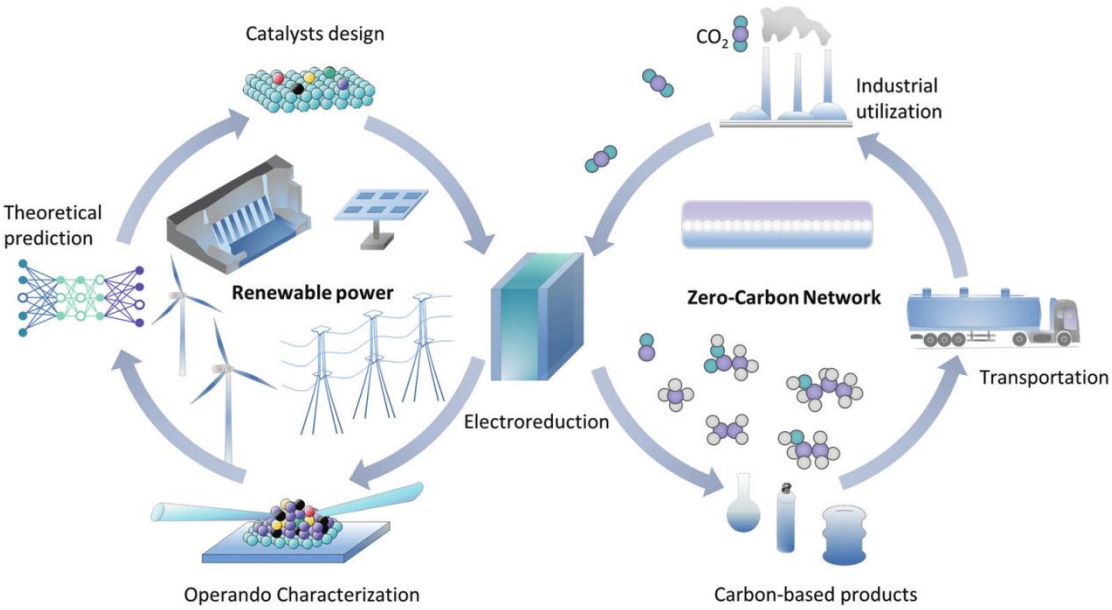

Figure 2. Schematic of the carbon cycle via CO_2 electrolysis, driven by renewably generated electricity [8].

1.1 Background of ECR to Multi-Carbon Products

Converting CO_2 into high value-added chemicals is particularly desirable [11]. In comparison to methane (CH_4) [12, 13], carbon monoxide (CO) [14-18], or formic acid [19, 20] (HCOOH or formate ($HCOO^-$) in alkaline electrolyte) that are the major C_1 products of CO_2 reduction, C_{2+} (encompassing two or more carbon atoms) hydrocarbons and oxygenates possess higher (volumetric and gravimetric) energy densities and greater economic value (as illustrated in Fig. 3) [21], and are in higher global demand. Ethylene (C_2H_4), for example, [22] is a versatile feedstock for producing plastics and diesel fuels, thus its selective production over C_1 products such as CH_4 is desirable. Ethanol (C_2H_5OH) [23] can be used as a high-octane fuel and also as a reactant for various other organic products.

However, efficient CO_2 reduction to higher-carbon products remains challenging for several reasons: 1) A severe parasitic proton reduction occurs at similar overpotentials. 2) The high C–C coupling energy cost and the competition of C–C bond formation with the formation of C–O and C–H bonds. 3) The large overpotential gap for the generation of CO intermediates and C_{2+} compounds. 4) An increase to the activation energy on metal surfaces that facilitate stronger

*CO binding (i.e., scaling relationships). Intermediates are required to be at the catalyst surface and in close proximity to one another for the second-order electron/proton coupling reactions to take place, which imposes constraints for C_{2+} production. Separating the resulting products from a catalyst with low selectivity, even if it also exhibits remarkable activity, brings significant additional costs.

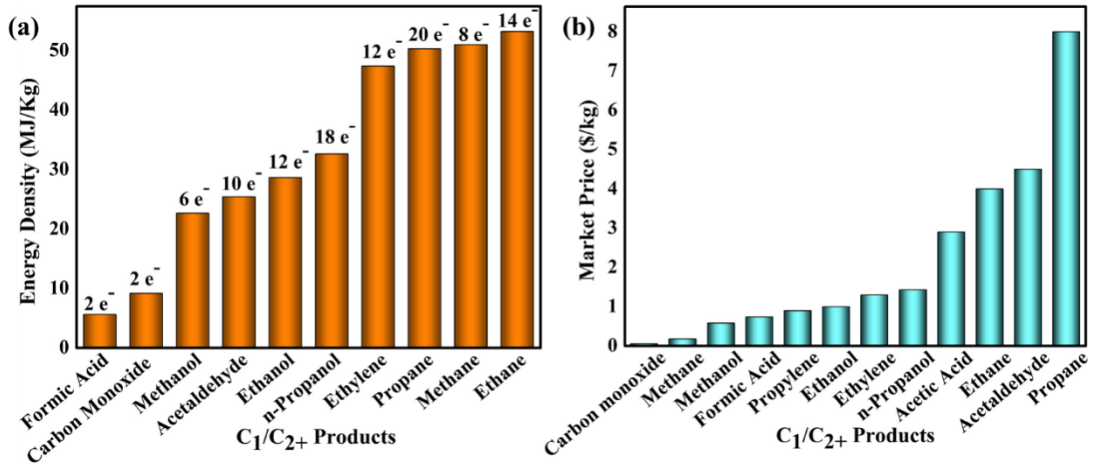

Figure 3. (a) Energy density and (b) market price of ECR products.

1.2. Uniqueness of Copper for ECR

Transition metals have available orbitals and active *d* electrons, which may energetically facilitate bond creation between the metal and ECR intermediates via *C or *O. Hori and co-workers classified single metal electrodes into four main groups, based on their favorability toward binding ECR and HER intermediates such as *OCHO (bound to the surface via oxygen), *COOH, (bound to the surface by carbon), *CO, and *H. Group 1 includes Hg, Sn, Pb, Tl, In, Cd, and Bi, which mainly yield HCOOH or $HCOO^-$, as the $CO_2^{\bullet-}$ intermediate is weakly stabilized by *OCHO or *COOH. Group 2 includes Ag, Zn, Pd, Au, and Ga, which generate CO as the major product due to the suitable *CO binding energies of these metals, as illustrated by the volcano plot in Fig. 4. Group 3 includes Ti, Pt, Ni, and Fe, which bind *CO too tightly, leading to poor CO desorption rate and CO poisoning. These mainly reduce water to H_2 and are not effective for ECR. Unlike the metals in Groups 1, 2, and 3, Cu alone belongs to

its own Group 4, and has been found to be the only metal that can catalyze the ECR to HCOOH, CO, and many other hydrocarbons of high carbon count, at reasonable faradaic efficiencies (FEs) [24]. Cu is unique due to its "ideal" binding strength toward *CO, following the Sabatier principle (Fig. 4), thus facilitating further stepwise transformation [25]. Specifically, the *CO generated on the surface does not have such weak affinity such that it instantly desorbs, and its affinity is not so strong as to poison the catalyst surface. In addition, Cu has a negative adsorption energy toward CO*, but a positive adsorption energy for H* (an intermediate in the competing hydrogen evolution reaction, HER) [26]. Note that twelve C_{2+} products on a Cu electrode have been identified [27]. Six products, including C_2H_4, C_2H_5OH, 1-propanol (*n*-C_3H_7OH), allyl alcohol (C_3H_5OH), acetaldehyde (CH_3CHO), and propionaldehyde (CH_3CH_2CHO), have been commonly reported in previous studies [28-30]. Acetic acid (CH_3COOH) has appeared in only a few reports [31-33]. The five remaining multi-carbon products, ethylene glycol ($HOCH_2CH_2OH$), glycolaldehyde ($HOCH_2CHO$), hydroxyacetone (acetol, $CH_3C(O)CH_2OH$), acetone (CH_3COCH_3) [34], and glyoxal (OCHCHO) have only been rarely reported.

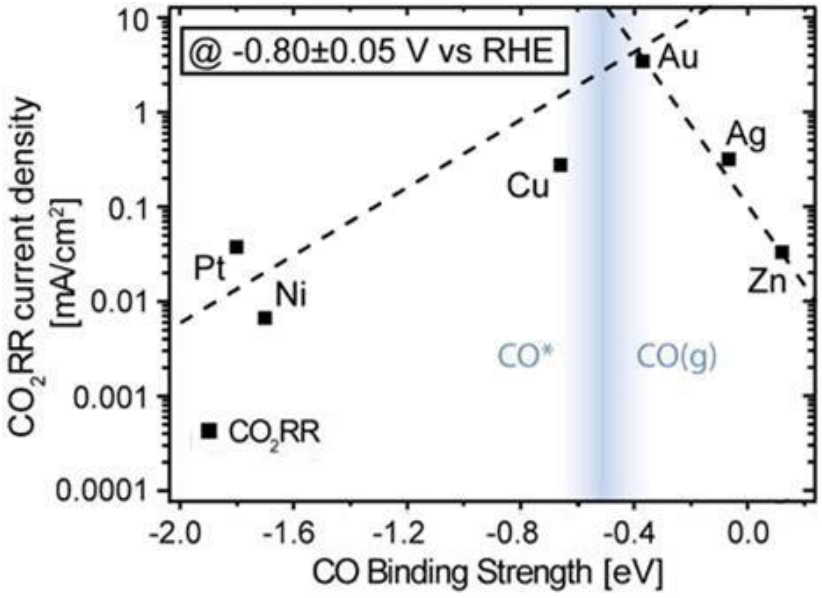

Figure 4. Volcano plot of the CO binding strength versus partial current density for ECR at –0.8 V. A vertical line labeled CO*|CO(g) indicates the

thermodynamics of chemical CO adsorption/desorption. Reprinted from Kuhl et al. [25] with permission. Copyright 2020 WILEY-VCH Verlag GmbH & Co. KGaA, Weinheim.

Despite the rapid progress that has been made in ECR after decades of exploration, large-scale implementation of this technology in a viable way that is competitive to conventional chemical synthesis processes still needs to overcome key hurdles, such as the large kinetic overpotential (up to 1.0 V for the more desirable C_{2+} products), insufficient current density (lower than that of commercial electrolyzers operated at 200 mA cm^{-2}), poor selectivity for C_{2+} production, and unsatisfactory long-term stability (loss of activity in less than 100 h as a result of poisoning by heavily adsorbed intermediates, byproducts, impurities, or degradation of electrocatalysts) [27]. To promote the viability of CO_2 electrolysis from a commercial perspective, the conversion rates and efficiencies must be boosted by more than an order of magnitude. Furthermore, the key intermediates, the origin of selectivity, and the reaction paths of the ECR process seem to be subtly different between materials, and have yet to be fully understood.

1.3. Focal Topics

Recent excellent perspectives on both heterogeneous and homogenous ECR are available [26, 35–38], and readers are encouraged to refer to these reviews to supplement the developments we describe. Given recent and significant advances regarding ECR, this article aims to provide a comprehensive and timely review of the different strategies that have been developed thus far to tune product selectivity, stability, and efficiency toward C_{2+} using Cu-based electrocatalysts. The correlations between structure and performance for efficient electrocatalyst designs are examined. Some key intermediate species are highlighted that shed light on CO_2 reduction pathways. We will also discuss the application of in situ and operando spectroscopy, along with computational techniques, that allow us to drastically improve our fundamental understanding of ECR. An outlook

exploring future opportunities and challenges in the conversion of CO_2 into multi-carbon fuels by Cu-based electrocatalysts is also presented.

2. Fundamentals of Electrochemical CO_2 Reduction

2.1. Thermodynamics and Kinetics of CO_2 Reduction

As an aqueous heterogeneous catalytic process, ECR consists of a two-electron or a multi-electron and proton process at a complex three-phase gas/solid/liquid interface at the electrode surface, which is also accompanied by the competitive HER. Three main steps describe the ECR reaction: 1) The dissolved CO_2 combines with the catalyst on the surface of the electrode by chemisorption. 2) Electrons or protons in the solution react with the adsorbed CO_2 molecules, breaking the carbon-oxygen bonds or forming carbon-hydrogen bonds. 3) The intermediates continue to accept electron-proton pairs and undergo molecular rearrangement to yield the final product. The product molecules then desorb from the catalyst surface and diffuse into the electrolyte [39–41].

It is difficult to diagnose the overall ECR mechanism because of the interlinked roles of both the CO_2 and water molecules, which increases the complexity of the mechanism, and because it occurs via multiple reaction steps [42]. The activation of the CO_2 molecule, the first step in the ECR, causes CO_2 to lose an electron to generate $CO_2^{\bullet-}$. However, this step requires a high reduction potential, with an aprotic solvent such as dimethylformamide reaching −1.97 V (versus standard hydrogen electrode, *vs.* SHE) [43], and a neutral aqueous solution as high as −1.9 V (*vs.* SHE). According to the number of electrons and protons transferred, the subsequent ECR pathways can be divided into two, four, six, eight, twelve, fourteen, and eighteen electrons, depending on the end product. Equations 1−24 summarize the electrochemical half-reactions of commonly reported ECR products in different solvents (Table 1). However, the ECR is in practice proton-dependent. In this case, the dependence of the pure $CO_2^{\bullet-}$ generation process on overcoming a high energy barrier can be avoided, so that the applied potential of ECR can be more positive, and thus lower the overall

power consumption [44].

Table 1. ECR reactions (equations (1)−(23)) and HER reaction (equation (24)) with standard reduction potentials in various solvents (all potentials are respect to normal hydrogen electrode (NHE) at pH 7).

Cathodic half reaction	Solvent	Standard reduction potential, E^0_{redox} (V)	Ref.
$CO_2 + 2H^+ + 2e^- \rightarrow HCOOH_{(aq)}$	H_2O	−0.61	1, 2
$CO_2 + 2H^+ + 2e^- \rightarrow CO_{(g)} + H_2O_{(l)}$	H_2O	−0.53 V	2, 3
$CO_2 + H_2O_{(l)} + 2e^- \rightarrow CO_{(g)} + H_2O_{(l)}$	H_2O	−1.35 V	3
$CO_2 + 2H^+_{(solv)} + 2e^- \rightarrow CO_{(g)} + H_2O_{(solv)}$	DMF	−1.77 V	4
	CH_3CN	−1.06 V, −1.16 V	4, 5
	DMF + HBF_4	−0.67 V	5
	DMF + 2 M H_2O	−1.1 V	5
$2CO_2 + 2H^+ + 2e^- \rightarrow H_2C_2O_{4(aq)}$	H_2O	−0.913 V	3
$2CO_2 + 2e^- \rightarrow C_2O_4^{2-}{}_{(aq)}$	H_2O	−1.003 V	3
$CO_2 + 4H^+ + 4e^- \rightarrow HCHO_{(l)} + H_2O_{(l)}$	H_2O	−0.48 V	3
$CO_2 + 3H_2O_{(l)} + 4e^- \rightarrow HCHO_{(l)} + 4OH^-$	H_2O	−1.31 V	3
$CO_2 + 6H^+ + 6e^- \rightarrow CH_3OH_{(l)} + H_2O_{(l)}$	H_2O	−0.38 V	2, 6
$CO_2 + 5H_2O_{(l)} + 6e^- \rightarrow CH_3OH_{(l)} + 6OH^-$	H_2O	−1.23 V	3
$CO_2 + 8H^+ + 8e^- \rightarrow CH_{4(g)} + 2H_2O_{(l)}$	H_2O	−0.24 V	2, 6
$CO_2 + 6H_2O_{(l)} + 8e^- \rightarrow CH_{4(g)} + 8OH^-$	H_2O	−1.07 V	3
$CO_2 + 8H^+_{(solv)} + 8e^- \rightarrow CH_{4(g)} + 2H_2O_{(solv)}$	CH_3CN	−0.89 V	7
$2CO_2 + 8H^+ + 8e^- \rightarrow CH_3COOH_{(g)} + 2H_2O_{(l)}$	H_2O	+0.23 V	2, 3
$2CO_2 + 12H^+ + 12e^- \rightarrow C_2H_{4(g)} + 4H_2O_{(l)}$	H_2O	−0.349 V	2, 6
$2CO_2 + 8H_2O(l) + 12e^- \rightarrow C_2H_{4(g)} + 12OH^-$	H_2O	−1.18 V	3
$2CO_2 + 12H^+ + 12e^- \rightarrow C_2H_5OH_{(l)} + 3H_2O_{(l)}$	H_2O	−0.329 V	2, 3
$2CO_2 + 9H_2O_{(l)} + 12e^- \rightarrow C_2H_5OH_{(l)} + 12OH^-$	H_2O	−1.16 V	3
$2CO_2 + 14H^+ + 14e^- \rightarrow C_2H_{6(g)} + 4H_2O_{(l)}$	H_2O	−0.27 V	2, 3
$3CO_2 + 18H^+ + 18e^- \rightarrow C_3H_7OH_{(l)} + 5H_2O_{(l)}$	H_2O	−0.31 V	2, 3
$2H^+ + 2e^- \rightarrow H_2$	H_2O	−0.42 V	3

According to the equation of $\Delta G = -nFE^0$ (n is the electron transfer number of the reduction reaction, and F is the Faraday constant, with value 96485 C mol^{-1}), the potential E^0 needs to be positive to make the cathodic reaction easier. Given the E^0 values listed in Table 1, the production of hydrocarbons or alcohols

are more thermodynamically favorable than that of CO, HCOOH, and H_2. However, this is not the case in practice since the ECR is also dependent on reaction kinetics associated with proton concentration and electron transport rate. This suggests that an active catalyst for ECR needs to possess an active site for both proton adsorption and rapid electron transfer.

2.2. Possible Reaction Pathways for the Formation of C_{2+} Products on Cu-Based Electrocatalysts

At present, HCOOH (or formate) and CO are the most common C_1 compounds produced from CO_2 reduction via a two-electron transfer process. In comparison, C_{2+} products offer larger volumetric energy densities and can act as building blocks for fabrication of long-chain hydrocarbon chemicals. However, the generation of C_{2+} compounds (e.g., C_2H_4, C_2H_5OH, CH_3COOH, and *n*-C_3H_7OH) relative to C_1 products requires the transfer of more electrons. In addition, it is challenging to elucidate the exact reaction mechanism during the ECR owing to the C–C bond formation competing with the generation of C–C, C–H, and C–O bonds. Therefore, to design and construct high-performance electrocatalysts, mechanistic understanding of reaction pathways for selective C–C bond formation is important.

The C–C bond coupling stage appears to be the most probable rate determining step (RDS) for the formation of C_2 and C_3 products. However, the C–C bond formation mechanism remains elusive. Based on a combination of controlled experiments and density functional theory (DFT) computations, four possible mechanisms were evaluated and summarized by Qiao and co-workers for the formation of C–C bonds, as depicted in Fig. 5 [52]. The top two mechanisms in Fig. 5, marked in blue, were originally proposed by Hori and coworkers [53]. Two $*CH_2$ species were suggested to directly dimerize to form C_2H_4 or through a Fischer-Tropsch like CO insertion pathway to yield $*CH_2CO$ and subsequently C_2H_4. The upright blue branch shows the direct dimerization of *CO to form *CO–CO, which was first investigated by DFT computations [54]. The bottom red

path provides the most highly probable route, suggesting that the negatively charged CO–CO species resulting from *CO dimerization coupled with an electron transfer is the RDS [55]. Following the proposal of these routes, a detailed summary of the overall map for most possible C_2 and C_3 pathways starting from *CO on Cu surfaces was constructed. The green route shown in Fig. 5 gives trace products (FE < 1%), including $HOCH_2CHO$ and $HOCH_2CH_2OH$, generated from an *CHO intermediate. The blue route leads to minor products (FE: 1−10%), including ethane (C_2H_6) and CH_3COO^-, originating from an adsorbed *COH intermediate. The red route yields major products, including C_2H_4, C_2H_5OH, and *n*-C_3H_7OH with an adsorbed *CO dimer as the precursor [52]. We will now briefly discuss the formation mechanism of the commonly reported C_{2+} products as below. Information about more complicated pathways can be found elsewhere [42, 56-58].

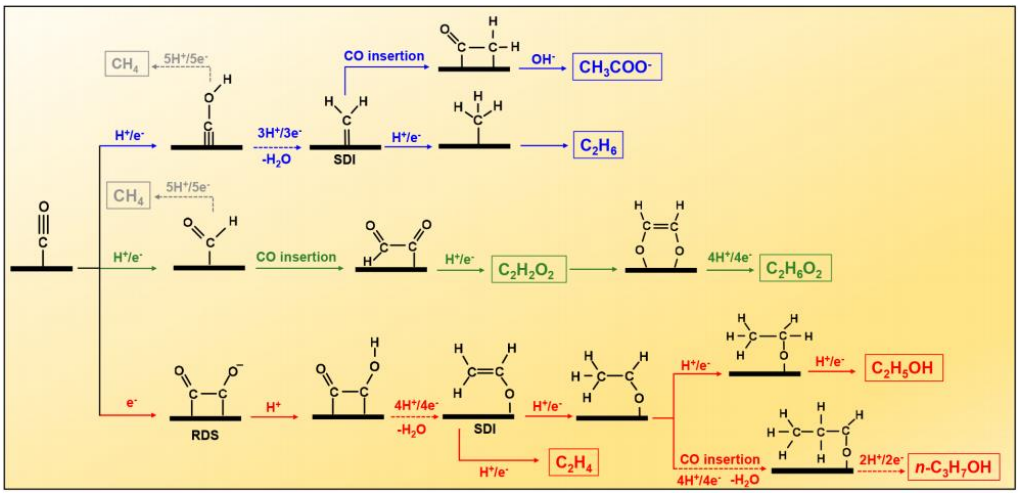

Figure 5. Most probable C_2 and C_3 formation routes starting from *CO on the surface of Cu. Reprinted from Zheng et al. [52] with permission. Copyright 2019 American Chemical Society.

2.2.1. Formation of C_2H_4

Among the different C_2 products, C_2H_4 is the simplest and has been the most studied. Several distinct pathways for C_2H_4 formation starting from *CO have been put forward, which mainly include *CO dimerization, *CO–COH coupling, and coupling of two *CH_2 species or CO insertion in a Fischer-Tropsch-like

manner [42]. Based on a combination of DFT computations, controlled experiments, and in situ/operando spectroscopy measurements, the *CO dimerization route is considered to be the most accepted C−C bond formation mechanism through a negatively charged CO−CO$^-$ species, which is then protonated to *CO−COH. It is then further reduced to *CH_2−CHO, a selectivity-determining intermediate (SDI) for C_2H_4 or CH_3CH_2OH. Cleavage of C−O gives rise to C_2H_4. Distinctly, CH_3CHO is obtained via protonation of the *a* carbon in *CH_2−CHO, which is further transformed into CH_3CH_2OH via *CH_3CH_2O. It was calculated that the C_2 pathways are limited by the 2*CO → *CO−COH step for strong binding of CO−CO$^-$. For weak CO−CO$^-$ binding, the step of *CH_2CHO → *O + C_2H_4 controls the C_2H_4 formation whereas the process of *CH_2CHO → *CH_3CHO → *CH_3CH_2O limits the C_2H_5OH formation. The formation of C_2H_5OH via *CH_3CHO was estimated to require a higher energetic barrier (~ 0.2 eV) than the formation of C_2H_4 from the reduction of *CH_2CHO [59]. In the carbene reaction pathway proposed by Hori et al., *CH_2 is the SDI for different C_2 products. Two *CH_2 species can combine to give C_2H_4. Alternatively, CO can insert into *CH_2 via a Fischer −Tropsch like manner to generate *CH_2CO and then to C_2H_4.

2.2.2. Formation of OCHCHO ($C_2H_2O_2$)

$C_2H_2O_2$ has been proposed to be generated from the insertion of CO into *CHO. Most of the $C_2H_2O_2$ formed does not desorb from the surface during the ECR, and is instead further reduced to other C_2 compounds (e.g., CH_3CH_2OH, $HOCH_2CH_2OH$, and CH_3CHO) on Cu. $C_2H_2O_2$ has been proposed to be a C_{2+} intermediate, and has been identified experimentally [60, 61]. As a result, only trace amounts of $C_2H_2O_2$ can be detected during the ECR.

2.2.3. Formation of C_2H_5OH

The production of C_2H_5OH shares similar pathways and intermediates (e.g., *COCHO with infrared-active vibrational frequencies at 1526 and 1291 cm^{-1}) with C_2H_4. At low overpotentials, dimerization of two *CO species to form

*$C_2O_2^-$ is the key step for C–C coupling to yield C_2H_5OH. *$C_2O_2^-$ is easily converted into *CO–COH and further reduced to vinyl alcohol (*CH_2=CHO) [63]. Protonation of the α carbon in *CH_2=CHO produces *CH_3CHO and then to C_2H_5OH via an ethoxy (*CH_3CH_2O) [55]. Another possible path to form C_2H_5OH arises from the formation of $C_2H_2O_2$, which is eventually reduced to C_2H_5OH at more negative overpotentials (< −0.6 V *vs*. RHE) [63].

2.2.4. Formation of $HOCH_2CH_2OH$ ($C_2H_6O_2$)

$C_2H_6O_2$ may be produced via a *CHO pathway, originating from *OCHCHO and subsequently *$HOCH_2CHO$. In contrast to CH_3CHO, OCHCHO, and $HOCH_2CHO$ that are reduced to other C_2 products on Cu, $C_2H_6O_2$ is not further reduced under similar conditions.

2.2.5. Formation of CH_3COOH (CH_3COO^-)

Five pathways have been proposed for CH_3COOH (CH_3COO^-) formation from CO_2 reduction. Coupling of two *CH_3CHO can produce CH_3COOH via Cannizzaro-type disproportionation reactions. This route demands very negative applied potentials from −1.5 V to −2.0 V (*vs*. RHE). A local alkaline environment with OH^- ions is speculated to promote the aldehyde disproportionation. Isomerization of *OCH_2COH to an epoxy compound followed by further reduction can give rise to CH_3COOH [63, 64].

Alternatively, CH_3COOH may be generated from a nucleophilic attack of *CH_3 species by the not adsorbed $CO_2^{\bullet-}$ [65]. If the kinetics for $CO_2^{\bullet-}$ formation and/or C−C coupling is more rapid than $CO_2^{\bullet-}$ protonation (to yield HCOOH), two $CO_2^{\bullet-}$ anions may combine to produce *OOCCOO, which is further protonated and reduced to CH_3COOH, as has been identified on N-doped nanodiamond/Si rod arrays by using in situ Fourier transform infrared (FTIR) spectroscopy. Among other suggestions, it was hypothesized that coupling of *CH_3O (arising from protonation of *CO) with $CO_2^{\bullet-}$ can generate CH_3COOH in 1-ethyl-3-methyl imidazolium tetrafluoroborate ([Emim]BF_4)-LiI aqueous

electrolytes on Cu(I)/C doped boron nitride [66]. This pathway needs the addition of strong Lewis acidic sites (Li^+) and nucleophilic sites (I^-). Their roles in the ECR should be further explored.

2.2.6. Formation of C_2H_6

Production of C_2H_6 thus far has only been occasionally observed, specifically on roughened Cu surfaces, $PdCl_2$-modified Cu electrodes, or nanostructured Cu_2O-derived Cu [67-69]. By studying CO_2 reduction on oxide-evolved Cu of varying thicknesses and oxidation states, Handoko et al. posited that C_2H_6 was formed through dimerization of two $*CH_3$ species and the $*CH_2$ intermediate was considered to be the SDI [70]. However, the absence of CH_4 on the electrodes where C_2H_6 is generated implies that it is unlikely C_2H_6 results from $*CH_3$, which is believed to be an intermediate for CH_4 formation [64]. It is thus supposed that C_2H_6 originates from the reduction of C_2H_4. This suggests the importance of atomically adsorbed hydrogen for C_2H_6 formation.

2.2.7. Formation of n-C_3H_7OH

Explicit mechanistic pathways to produce *n*-C_3H_7OH with high energy-mass density and octane number are still not well understood. It is kinetically difficult because the process requires transfer of eighteen e^- and eighteen H^+, and involves the formation of two C−C bonds. Stabilizing high coverage of C_2 (e.g., *CO–CO) species is considered to be key to facilitating *n*-C_3H_7OH formation [71]. Electrochemical tests and in situ/operando spectroscopy measurements indicate that the adsorbed C_2 intermediate (e.g., $*CH_3CHO$ from $*CH_2CHO$ or $*CH_3CH$ from $*CH_3CHO$) can couple with a neighboring C_1 intermediate (*CO) followed by proton/electron transfers to yield CH_3CH_2CHO (reminiscent of the hydroformylation of C_2H_4 with CO and H_2), and subsequently *n*-C_3H_7OH [53, 72].

2.2.8 Formation of Propylene (C_3H_6)

Production of one C_3H_6 molecule requires the transfer of eighteen electrons. Cu nanocrystals composed of Cu(100) and Cu(111) facets are suggested to favor

the binding of the critical *C_1 (e.g., *CO) and *C_2 (e.g., *$OCH=CH_2$) species toward C_3H_6 formation [73]. Specifically, adsorbed C_2 intermediates *$OCH=CH_2$ couple with either CO_2 molecules or *COOH to form *$C(OH)_2CH=CH_2$ and then to *$HCOHCH=CH_2$. The intermediate can be transformed into an ally alcohol ($HOCH_2CHCH_2$), which is then reduced to C_3H_6. Alternatively, *$HCOHCH=CH_2$ can be converted to C_3H_6 after being subjected to two proton-coupled electron transfer steps.

2.3. Application of In Situ Studies for CO_2 Reduction

Recent studies have shown that ECR catalysts may be continuously undergoing reconstruction under realistic operating conditions, which makes it difficult to identify true active sites and monitor their evolution through conventional characterization techniques, resulting in controversy about active sites and reaction mechanisms for the ECR. To avoid this ambiguity, identifying the reaction intermediates and catalytic products while under experimental conditions and in real-time is the key to reliably diagnosing the reaction mechanism and thus further optimizing catalytic performance. Therefore, it is necessary to monitor the dynamic evolution of the catalyst and reaction intermediates under experimental conditions by in-situ characterization technology.

2.3.1. In Situ Characterization Techniques for Catalyst Evolution Studies

Catalysts play an essential role in the whole process of ECR. During the catalysis process, the catalyst itself may undergo changes including phase transformation, alteration of valence states, morphology and local coordination environment, etc. In order to inform the design of desired optimized catalysts, in situ characterization techniques have been applied to monitor the catalyst evolution process. In situ X-ray diffraction (XRD) can be used to monitor the phase transformation of a catalyst, and the valence state change of a catalyst can be detected by using in situ X-ray photoelectron spectroscopy (XPS). Compared

to phase transformation and valence states, it is more difficult to monitor morphology evolution, local coordination environment changes, electron transfer behaviors, and real active sites in catalysts in real-time. In this case, the appearance of in situ environmental transmission electron microscopy (TEM) opens up possibilities for directly observing the dynamic changes of catalyst morphology, and then in situ X-ray absorption spectroscopy (XAS) can monitor local coordination environment of catalysts. As for electron-transfer behavior and the active sites, it is necessary to combine with various in situ characterization techniques. For instance, in situ XPS could reveal the electron-transfer direction, and in situ electron spin resonance (ESR) measurements could be used to unveil the real active sites.

2.3.2. In Situ Characterization Techniques for Reaction Intermediates Studies

To better understand the reaction mechanism, in situ UV−vis spectroscopy, XPS techniques, in situ Raman spectroscopy, and in situ FTIR spectroscopy can be used for detecting reaction intermediates in real time. Ma et al. employed in situ FTIR spectroscopy to verify a hydrogen-assisted C–C coupling mechanism, in which the adsorbed *CO and *CHO species are key intermediates and the in situ FTIR results provided experimental evidence for the hydrogen-assisted C–C coupling mechanism.

2.*3.3. In Situ Characterization Techniques for Catalytic Products Studies*

As for understanding the ECR process, the real-time characterization of catalytic products cannot be ignored, particularly for evaluating the electrocatalyst performance and revealing the catalytic mechanism under different reaction conditions. Therefore, in situ online electrochemical mass spectrometry (MS) has been used to determine the catalytic products. For example, Wadayama et al. designed an electrochemical setup for in situ MS to continuously measure the evolved products from ECR. The CO_2 gas was kept inside the in situ cell atmosphere with Ar as carrier gas, and the catalyst was

cycled in the potential range from −0.4 to −1.4 V (*vs*. RHE). The in situ MS results showed that the yield of products depends on the applied potentials and the catalyst's exposed crystal planes.

2.4. Cu-Based Catalysts for CO_2 Reduction to C_{2+} Products

We have summarized the maximum FEs against corresponding overpotentials and the total current density for about 380 reported ECR catalysts in order to provide a visual illustration of the latest trend of product generations via ECR with Cu-based catalysts, as presented in Fig. 6 and Table S1. Note that $2e^-$ products (CO and $HCOO^-$) can be produced with FEs > 90%, requiring less overpotential for CO, but have only limited current density [74-77]. Modest FEs ranging from 30% to 80% were attained for the formation of CH_4 [12, 13, 78], methanol (CH_3OH) [79, 80], CH_3COOH [81], C_2H_4 [28, 82], and C_2H_6 [83]. Meanwhile, the current density during the generation of these products is relatively higher compared to $2e^-$ products (CO and $HCOO^-$) because the applied potential range is wider. Among these products, CH_3OH displays a strikingly smaller overpotential than the others, whereas higher e^- products (CH_4 and C_2H_4) require an overpotential of up to 1.0 V with scattered efficiency. C_2H_5OH and *n*-propanol (*n*-C_3H_7OH) were generated with substantially lower FEs (< 52%) while demanding higher overpotentials than CH_3OH [29, 30]. The FE for others C_3 products is even less than 10% [34].

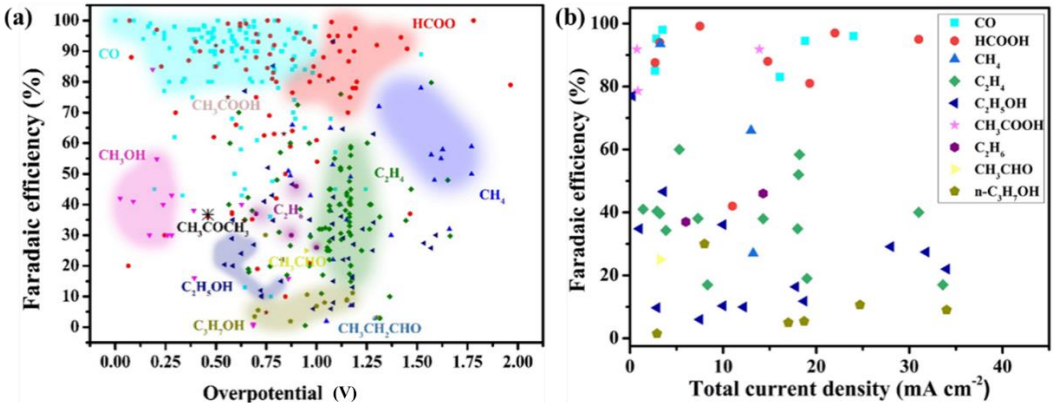

Figure 6. (a) Maximum FE of ECR products against their respective overpotential for the 380 reported catalysts included in Table S1 (Supporting

Information). The background color intensity correlates with the density of points to guide the eye. (b) Maximum ECR FE versus total geometry current density.

We have summarized the performance of Cu-based catalysts for ECR toward C_{2+} products in Table 2. Insight into reactive sites, reaction paths, and tunability of Cu is still urgently needed in many of the reports.

Table 2. Summary of the activity of Cu-based electrocatalysts for ECR toward C_{2+} compounds in different electrolytes.

Catalyst	Electrolyte	J (mA·cm^{-2})	Onset potential (V) or η (V)	Main product, FE	Ref.
Surface reconstructed Cu	0.05 M $KHCO_3$	17 mA cm^{-2} @ −2.6 V *vs*. RHE	N/A	C_2H_4, 56%; *n*-C_3H_7OH, 5% @ −2.6 V *vs*. RHE	84
Porous Cu films	0.1 M $KHCO_3$	~ 18 mA cm^{-2} @−1.38 V *vs*. RHE	N/A	C_2H_4, 34.8 % @ −1.38 V *vs*. RHE	85
ERD Cu	0.1 M $KHCO_3$	31 mA cm^{-2} @ −1.2 V *vs*. RHE	N/A	C_2H_4, 40% @ −1.2 V *vs*. RHE	86
Plasma oxidized Cu	0.1 M $KHCO_3$	N/A	Onset potential, -0.5 V *vs*. RHE	C_2H_4, 60% @ −0.9 V *vs*. RHE	87
Anodized Cu	0.1 M $KHCO_3$	7.3 mA cm^{-2} @ −1.08 V *vs*. RHE	N/A	C_2H_4, 38.1 % @ −1.08 V *vs*. RHE	88
Cu mesocrystals	0.1 M $KHCO_3$	N/A	N/A	C_2H_4, 27.2% @ −0.99 V *vs*. RHE	89
Cu/OLC	0.1 M $KHCO_3$	5.3 mA cm^{-2} @ −1.8 V *vs*. Ag/AgCl	Onset potential, ~ −1.4 V *vs*. Ag/AgCl	C_2H_4, 60% @ −1.8 V *vs*. Ag/AgCl	90
CuAg	0.1 M $KHCO_3$	18.1 mA cm^{-2} @ −1.05 V *vs*. RHE	N/A	C_2H_4, 52% @ −1.05 V *vs*. RHE	22
CuO_x-Vo	0.1 M $KHCO_3$	~ 30 mA cm^{-2} @ −1.4 V *vs*. RHE	Onset potential, −0.6 V *vs*. RHE	C_2H_4, 63% @ −1.4 V *vs*. RHE	91
Boron-doped CuO nanobundles	0.1 M $KHCO_3$	18.2 mA cm^{-2} @ −1.1 V *vs*. RHE	N/A	C_2H_4, 58.4% @−1.1 V *vs*. RHE	92
Branched CuO	0.1 M $KHCO_3$	19.2 mA cm^{-2} @	N/A	C_2H_4, 76% @	93

nanoparticles (NPs)		−1.05 V *vs*. RHE		−1.05 V *vs*. RHE	
Amorphous Cu NPs	0.1 M $KHCO_3$	N/A	N/A	C_2H_5OH, 22% @ −1.05 V *vs*. Ag/AgCl	94
OD Cu/C	0.1 M $KHCO_3$	1.0 mA cm^{-2}@ −0.5 V *vs*. RHE	Onset potential, ~ −0.1 V *vs*. RHE	C_2H_5OH, 34.8% @ −0.7 V *vs*. RHE	95
Cu/C_3N_4	0.1 M $KHCO_3$	~ 7.5 mA cm^{-2} @ −1.6 V *vs*. Ag/AgCl	Onset potential, ~ −0.75 V *vs*. RHE	C_2H_5OH, 6% @ −1.6 V *vs*. Ag/AgCl	96
Cu_5Zn_8	0.1 M $KHCO_3$	2.3 mA cm^{-2} @ −0.8 V *vs*. RHE	N/A	C_2H_5OH, 46.6% @ −0.8 V *vs*. RHE	97
OD-Cu_4Zn	0.1 M $KHCO_3$	28 mA cm^{-2} @ −1.05 V *vs*. RHE	N/A	C_2H_5OH, 29.1% @ −1.05 V *vs*. RHE	98
Cu NFs (I)	0.1 M $KHCO_3$	N/A	N/A	C_2H_6, 30% @ −0.74 V *vs*. RHE	99
Cu_2O-derived Cu	0.1 M $KHCO_3$	N/A	N/A	C_2H_6, 30.1% @ −1.0 V *vs*. RHE	67
Au-bipy-Cu	0.1 M $KHCO_3$	3.25 mA cm^{-2} @ −0.9 V *vs*. RHE	N/A	CH_3CHO, 25% @ −0.90 V *vs*. RHE	24
Cu nanocubes (NCs)	0.1 M $KHCO_3$	24.7 mA cm^{-2} @ −0.95 V *vs*. RHE	Onset potential, −0.75 V *vs*. RHE	*n*-C_3H_7OH, 10.6% @ −0.85 V *vs*. RHE	100
Cu nanodendrites	0.1 M $KHCO_3$	N/A	Onset potential, −1.0 V *vs*. RHE	CH_3CH_2CHO, 2.9% @ −1.2 V *vs*. RHE	101
Cu-SA/NPC	0.1 M $KHCO_3$	N/A	Onset potential, −0.25 V *vs*. RHE	CH_3COCH_3, 36.7% @ −0.36 V *vs*. RHE	34
Nanoporous Cu films	0.1 M $KHCO_3$	14.3 mA cm^{-2} @ −1.7 V *vs*. NHE	Onset potential (C_{2+} products), −0.96 V *vs*. NHE	C_2H_4, 38% (30 × 40 nm pores); C_2H_6, 46% (30 × 70 nm pores) @ −1.7 V *vs*. NHE	102
Cu_2O derived Cu NPs	0.1 M $KHCO_3$	N/A	N/A	C_2H_4, 19%; C_2H_6, 6% @ −1.1 V *vs*. RHE	64

3.6-μm Cu_2O films	0.1 M $KHCO_3$	17.8 mA cm^{-2} @ −0.99 V *vs.* RHE	N/A	C_2H_4, 34.26%; C_2H_5OH, 16.37% @ −0.99 V *vs.* RHE	103
Cu(100) single crystals	0.1 M $KHCO_3$	N/A	N/A	C_2H_4, 27%; C_2H_5OH, 32% @ Pulsed	104
Cu nanowire arrays	0.1 M $KHCO_3$	N/A	N/A	C_2H_4, 17.4%; *n*-C_3H_7OH, 8% @ −1.1 V *vs.* RHE	105
Plasma-Cu nanocubes	0.1 M $KHCO_3$	~ 34 mA cm^{-2} @ −1.0 V *vs.* RHE	N/A	C_2H_4, 45%; C_2H_5OH, 22%; *n*-C_3H_7OH, 9% @−1.0 V *vs.* RHE	106
Cu(100) single electrode	0.1 M $KHCO_3$	2.9 mA cm^{-2} @ −1.0 V *vs.* RHE	N/A	C_2H_4, 40.4%; C_2H_5OH, 9.7%; *n*-C_3H_7OH, 1.5% @ −1.0 V *vs.* RHE	107
18-nm Cu	0.1 M $KHCO_3$	18.7 mA cm^{-2} @ −1.03 V *vs.* RHE	N/A	C_2H_4, 42.6%; C_2H_5OH, 11.8%; *n*-C_3H_7OH, 5.4% @ −1.03 V *vs.* RHE	108
Cu-on-Cu_3N	0.1 M $KHCO_3$	N/A	N/A	C_2H_4, 39%; C_2H_5OH, 19%; *n*-C_3H_7OH, 6% @ −0.95 V *vs.* RHE	109
$Cu_{28}Ag_{72}$	0.1 M $KHCO_3$	N/A	N/A	C_2H_4, 12.8%; C_2H_5OH, 17.3%; CH_3CHO, 24.1% @ Pulse	110
Electropolished Cu foil	0.1 M $KHCO_3$	2.8 mA cm^{-2} @ −1.05 V *vs.* RHE	N/A	C_{2+} products, 40.6% @ −1.05 V *vs.* RHE	27
Porous Cu nanoribbons	0.1 M $KHCO_3$	~ 5 mA cm^{-2} @ −0.701 V *vs.* RHE	Onset potential (C_2H_4), ~ −0.63 V *vs.* RHE	C_{2+} products, 40% @ −0.816 V *vs.* RHE	111
Packed Cu NPs	0.1 M $KHCO_3$	10 mA cm^{-2} @ −0.75 V *vs.* RHE	Onset potential, −0.53 V *vs.* RHE	C_{2+} products, 50% @ −0.75 V *vs.* RHE	112

Cu(100)	0.1 M $KHCO_3$	2 mA cm^{-2} @ −0.97 V *vs*. RHE	N/A	C_{2+} products, 60% @ −0.97 V *vs*. RHE	[113]
Prism Cu	0.1 M $KHCO_3$	10 mA cm^{-2} @ −1.1 V *vs*. RHE	N/A	C_{2+} products, 35% @ −1.1 V *vs*. RHE	[114]
PcCu-Cu-O	0.1 M $KHCO_3$	7.3 mA cm^{-2} @ −1.2 V *vs*. RHE	N/A	C_2H_4, 51% @ −1.2 V *vs*. RHE	[115]
$Cu/CuSiO_3$	0.1 M $KHCO_3$	20.2 mA cm^{-2} @ −1.1 V *vs*. RHE	N/A	C_2H_4, 51.8% @ −1.1 V *vs*. RHE	[116]
Cu-Ag	0.1 M $KHCO_3$	2.5 mA cm^{-2} @ −1.4 V *vs*. RHE	N/A	C_2H_5OH, 23.1% @ −1.4 V *vs*. RHE	[117]
Cu KBr	0.1 M $KHCO_3$	22.06 mA cm^{-2} @ −1.1 V *vs*. RHE	N/A	C_2H_4, 50.94% @ −1.1 V *vs*. RHE	[118]
Double sulfur vacancy-rich CuS	0.1 M $KHCO_3$	9.9 mA cm^{-2} @ −0.85 V *vs*. RHE	N/A	*n*-C_3H_7OH, 15.4% @ −1.05 V *vs*. RHE	[119]
Cu/NPC-800	0.2 M $KHCO_3$	N/A	N/A	C_2H_5OH, 64.6% @ −1.05 V *vs*. RHE	[121]
100-cycles Cu	0.25 M $KHCO_3$	52 mA cm^{-2} @ −1.2 V *vs*. RHE	Onset potential (C_2H_4), -0.7 V *vs*. RHE	C_{2+} products, 73% @ −1.2 V *vs*. RHE	[122]
Cu NPs/NG	0.5 M $KHCO_3$	19.0 mA mg^{-1} @ −1.2 V *vs*. NHE	Onset potential, −0.7 V *vs*. NHE	C_2H_4, 19% @ −0.9 V *vs*. NHE	[123]
Cu mesh	0.5 M $KHCO_3$	3.87 mA cm^{-2} @ −1.1 V *vs*. RHE	Onset potential, ~ −0.7 V *vs*. RHE	C_2H_4, 34.3% @ −1.1 V *vs*. RHE	[124]
CuO-PVDF	0.5 M $KHCO_3$	11.7 mA cm^{-2} @ −1.12 V *vs*. RHE	N/A	C_2H_4, 40.6% @ −1.22 V *vs*. RHE	[125]
HKUST-1	0.5 M $KHCO_3$	10 mA cm^{-2} @ −0.9 V *vs*. Ag/AgCl	Onset potential, < −1.0 V *vs*. Ag/AgCl	C_2H_5OH, 10.3% @ −0.9 V *vs*. Ag/AgCl	[126]
N-ND/Cu	0.5 M $KHCO_3$	N/A	N/A	CH_3COOH, 34.7% @ −0.5 V *vs*. RHE	[127]

Cu_4O	0.5 M $KHCO_3$	44.7 mA cm^{-2} @ −1.0 V *vs.* RHE	N/A	C_2H_4, 45% @ −0.9 V *vs.* RHE	128
CuAu	0.5 M $KHCO_3$	N/A	N/A	C_2H_4, ~ 18% @ −0.6 V *vs.* RHE	129
Cu-12	1.0 M $KHCO_3$	232 mA cm^{-2} @ −0.83 V *vs.* RHE	N/A	C_2H_4, 72% @ −0.83 V *vs.* RHE	130
Hydrophobic Cu dendrites	0.1 M $CsHCO_3$	N/A	N/A	C_2H_4, 56%; C_2H_5OH, 17% @ 30 mA cm^{-2}	131
OD-Cu	0.1 M $CsHCO_3$	13.3 mA cm^{-2} @ −1.0 V *vs.* RHE	N/A	C_{2+} products, 70% @ −1.0 V *vs.* RHE	132
Cu/THH Pd NCs	0.1 M $NaHCO_3$	N/A	N/A	C_2H_5OH, 20.4% @ −0.46 V *vs.* RHE	133
GN/ZnO/Cu_2O	0.5 M $NaHCO_3$	8.0 mA cm^{-2} @ −1.8 V *vs.* Ag/AgCl	N/A	*n*-C_3H_7OH, 30% @ −0.9 V *vs.* Ag/AgCl	134
Cu skeletons	0.5 M $NaHCO_3$	N/A	Onset potential, −0.25 V *vs.* RHE	C_{2+} products, 32.2% @ −1.1 V *vs.* RHE	135
Cu foams	0.5 M $NaHCO_3$	N/A	Onset potential, −0.4 V *vs.* RHE	C_2H_6, 37% @ −0.7 V *vs.* RHE	136
Cu/G	0.5 M $NaHCO_3$	12.2 mA cm^{-2} @ −1.7 V *vs.* Ag/AgCl	N/A	C_2H_5OH, 9.93% @ −0.9 V *vs.* Ag/AgCl	137
CuPd	0.25 M K_2CO_3	33.6 mA cm^{-2} @ −1.4 V *vs.* Ag/AgCl	N/A	C_2H_4, ~ 17% @ −1.4 V *vs.* Ag/AgCl	138
CuO	0.2 M KI	10 mA cm^{-2} @ −1.49 V *vs.* SCE	N/A	C_2H_5OH, 36.1% @ −1.7 V *vs.* SCE	139
Cu NPs/TiO_2	0.2 M KI	31.79 mA cm^{-2} @ −1.45 V *vs.* RHE	Onset potential, -0.607 V *vs.* RHE	C_2H_5OH, 27.4% @ −1.45 V *vs.* RHE	140
Dendritic Cu	0.1 M KBr	N/A	N/A	C_2H_4, 57% @ 170 mA cm^{-2}	141
Boron-doped Cu	0.1 M KCl	70 mA cm^{-2} @ −1.1 V *vs.* RHE	Onset potential, −0.57 V *vs.* RHE	C_2H_4, 52%; C_2H_5OH, 27% @ −1.1 V *vs.* RHE	142

Ag-Cu_2O	0.2 M KCl	N/A	N/A	C_2H_4, 7.8%; C_2H_5OH, 20.1%; C_2H_6, 1.6% @ −1.2 V *vs*. RHE	[143]
Cu(II) phthalocyanine/C	0.5 M KCl	2.8 mA cm^{-2} @ −1.6 V *vs*. Ag/AgCl	N/A	C_2H_4, 25% @ −1.6 V *vs*. Ag/AgCl	[144]
Cu/Cu_xO	0.5 M KCl	N/A	N/A	C_2H_5OH, 42.4%; CH_3CHO, 13.7%; CH_3COCH_3, 7% @ −1.0 V *vs*. RHE	[145]
Cu_4O_3-rich catalyst	0.5 M Cs_2SO_4	~ 129 mA cm^{-2} @ −1.4 V *vs*. RHE	N/A	C_2H_4, ~ 43% @ −0.64 V *vs*. RHE	[146]
Fluorine-modified Cu	0.75 M KOH	1.6 A cm^{-2} @ −0.89 V *vs*. RHE	N/A	C_{2+} products, 80% @ −0.89 V *vs*. RHE	[147]
Nanoporous Cu films	1.0 M KOH	700 A g^{-1} @ −0.7 V *vs*. RHE	N/A	C_2H_4, 40%; C_2H_5OH, 20% @ −0.5 V *vs*. RHE	[148]
Cu NPs	1.0 M KOH	150 mA cm^{-2} @ −0.58 V *vs*. RHE	η, 0.14 V	C_2H_4, ~ 35% @ −0.58 V *vs*. RHE	[149]
Cu cubes	1.0 M KOH	200 mA cm^{-2} @ −0.7 V *vs*. RHE	N/A	C_2H_4, 60% @ −0.7 V *vs*. RHE	[150]
Nanoporous Cu	1.0 M KOH	411 mA cm^{-2} @ −0.67 V *vs*. RHE	N/A	C_2H_4, 38.6%; C_2H_5OH, 16.6%; *n*-C_3H_7OH, 4.5% @−0.67 V *vs*. RHE	[151]
34% N-C/Cu	1.0 M KOH	156 mA cm^{-2} @ −0.68 V *vs*. RHE	N/A	C_2H_5OH, 52% @ −0.68 V *vs*. RHE	[30]
CSVE-Cu	1.0 M KOH	120 mA cm^{-2} @ −0.92 V *vs* RHE	N/A	C_2H_5OH, 25%; *n*-C_3H_7OH, 7% @ −0.92 V *vs* RHE	[29]
CuAg wires	1.0 M KOH	265 mA cm^{-2} @ −0.68 V *vs*. RHE	N/A	C_2H_4, 60%; C_2H_5OH, 25% @ −0.68 V *vs*. RHE	[152]
20-50 nm phase-separated CuPd NPs	1.0 M KOH	~360.5 mA cm^{-2} @ −0.71 V *vs*. RHE	Onset potential, −0.3 V *vs*. RHE	C_2H_4, ~48%; C_2H_5OH, ~15% @ −0.74 V *vs*. RHE	[153]
CuSn	1.0 M KOH	225 mA cm^{-2} @ −0.8 V *vs*. RHE	N/A	C_2H_4, 60% @ −0.8 V *vs*. RHE	[154]

Cu-Al	1.0 M KOH	400 mA cm^{-2} @ −1.5 V *vs*. RHE	N/A	C_2H_4, 80% @ −1.5 V *vs*. RHE	28
CuAg-DAT	1.0 M KOH	N/A	N/A	C_2H_5OH, 25% @ −0.8 V *vs*. RHE	154
$Ce(OH)_x$/Cu/PTFE	1.0 M KOH	300 mA cm^{-2} @ −0.7 V *vs*. RHE	N/A	C_2H_5OH, 43% @ −0.7 V *vs*. RHE	23
Multi-hollow Cu_2O	2.0 M KOH	71.8 mA cm^{-2} @ −0.61 V *vs*. RHE	N/A	C_2H_5OH, 26.9% @ −0.61 V *vs*. RHE	155
Graphite/carbon NPs/Cu/PTFE	7.0 M KOH	100 mA cm^{-2} @ −0.55 V *vs*. RHE	NA	C_2H_4, 70% @ −0.55 V *vs*. RHE	156
Cu-CO_2-60	7.0 M KOH	280 mA cm^{-2} @ −0.67 V *vs*. RHE	N/A	C_{2+} products, 90% @ −0.67 V *vs*. RHE	81
Cu(I)/BN-C	([Emim]BF_4)-LiI-water solution	13.9 mA cm^{-2} @ −2.2 V *vs.* Ag/Ag^+	η, 0.52 V @ 13.9 mA cm^{-2}	CH_3COOH, 91.8% @ −2.2 V *vs.* Ag/Ag^+	66

3. Catalyst Design to Make C_{2+} Production a Competitive Process

3.1. Surface Structure Tuning

3.1.1. Morphology

Different shapes of Cu materials, including nanowires, nanoparticles (NPs), core-shell and mesoporous foams have been shown to profoundly influence the ECR activity and selectivity by affecting the local pH or proton concentration on the surface of catalyst [157–159]. Thus tailoring the morphology of Cu-based materials provides an effective method to improve C_{2+} production via the ECR.

It is believed that *CO is the critical intermediate for the formation of C_{2+} compounds mainly either through dimerization (to form CO–CO) or coupling with *CHO (to form CO–COH) pathways. Both pathways need *CO to be abundant on the catalyst surface and in close proximity to each other. To this end, control of specific morphological and electronic characteristics is desired. For example, Wang et al. prepared several Cu-based nanomaterials with different morphologies that all used the same precursor (such as copper oxide) and compared their ECR performance under the same test conditions [160]. It was found that the onset potential for C_2 products changed significantly as the morphology

of copper catalysts varied from nanowire to nanoflower. In all tested Cu-based nanostructures, Cu nanosheets provided the highest catalytic activity, imparting a FE of 47.3% toward C_2 products at −0.4 V (*vs.* RHE). It was proposed that the nanosheet structure could better stabilize the intermediates of ECR, thus promoting the deep reduction of CO_2.

3.1.2. Particle Size

Reducing the size of metal NPs leads to creation of low-coordination sites apart from the original close-packed sites, which may influence the binding strength of reaction intermediates, thereby affecting the activity and selectivity of electrocatalysts. The size effect is due to a combination of two factors. First, the atom ratio increases if the particle size decreases, resulting in the curvature of its surface becoming larger and the average coordination of the surface atoms thus being lowered. The lower coordination number causes electron structure perturbation and thus increases the reactivity. Second, for a small particle, the strain of the material surface shifts the *d*-band and alters the reactivity [23].

Li et al. prepared monodispersed Cu NPs with different sizes assembled on a pyridinic-N rich graphene (p-NG), and observed a Cu NP size-dependent performance for ECR to C_2H_4 in 0.5 M $KHCO_3$ [123]. Compared to p-NG-Cu-7 (Cu NPs of 7 nm), p-NG-Cu-13 (Cu NPs of 13 nm) displayed a markedly lower C_2H_4 FE, which was ascribed to the larger Cu NP size.

3.1.3. Confinement

Space-confined catalysts are becoming a hot research field in ECR to produce hydrocarbons and oxygenates [161, 162]. Confined catalysts provide a relatively independent chemical environment separated from the bulk space by the nanoconfinement effect. In the specific isolated reaction region, the thermodynamics and kinetics of the reaction can be effectively controlled [163]. Compared with traditional catalysts, the selectivity to C_{2+} products of confined catalysts could be significantly improved [164, 165]. For instance, Mara et al.

designed a nanoparticle with an Ag core and a porous Cu shell for catalyzing ECR to C_{2+} products. CO_2 was reduced to *CO on the surface of Ag, which is confined in the channels of Cu, where coupling of two *CO occurred, leading to C_{2+} products (Fig. 7a) [166]. Recently, Sargent's group highlighted an enhanced space-confined ECR catalytic activity and selectivity [30]. A 200 nm Cu electrode was first coated onto a polytetrafluoroethylene (PTFE) membrane by magnetron sputtering. Subsequently, a nitrogen-doped carbon layer (N-C) and carbon layer (C) were covered on the surface of the pre-designed Cu electrode to obtain N-C/Cu and C/Cu electrodes, respectively (Fig. 7b). Among them, N-C/Cu and pure Cu electrodes were considered to be confined and unconfined catalysts, respectively. Catalytic tests showed that the confined catalyst exhibited a higher selectivity for C_2H_5OH products compared to the unconfined Cu electrode. The N-C/Cu electrode achieved a C_2H_5OH FE of 52% at a current density of 300 mA cm^{-2}, notably outperforming the unconfined Cu electrode with a C_2H_5OH FE of 30% (Fig. 7c). This enhancement was attributed to the observation that N-C/Cu has a certain electron-giving ability, and the CO (*CO) adsorbed on the surface of the Cu electrode received some electrons during the ECR process, thus reducing the energy barrier of the C–C coupling reaction. DFT calculations also indicated that the N-C/Cu electrode possessed a lower reaction energy barrier for the CO dimerization reaction, leading to a higher C_{2+} selectivity (Fig. 7d).

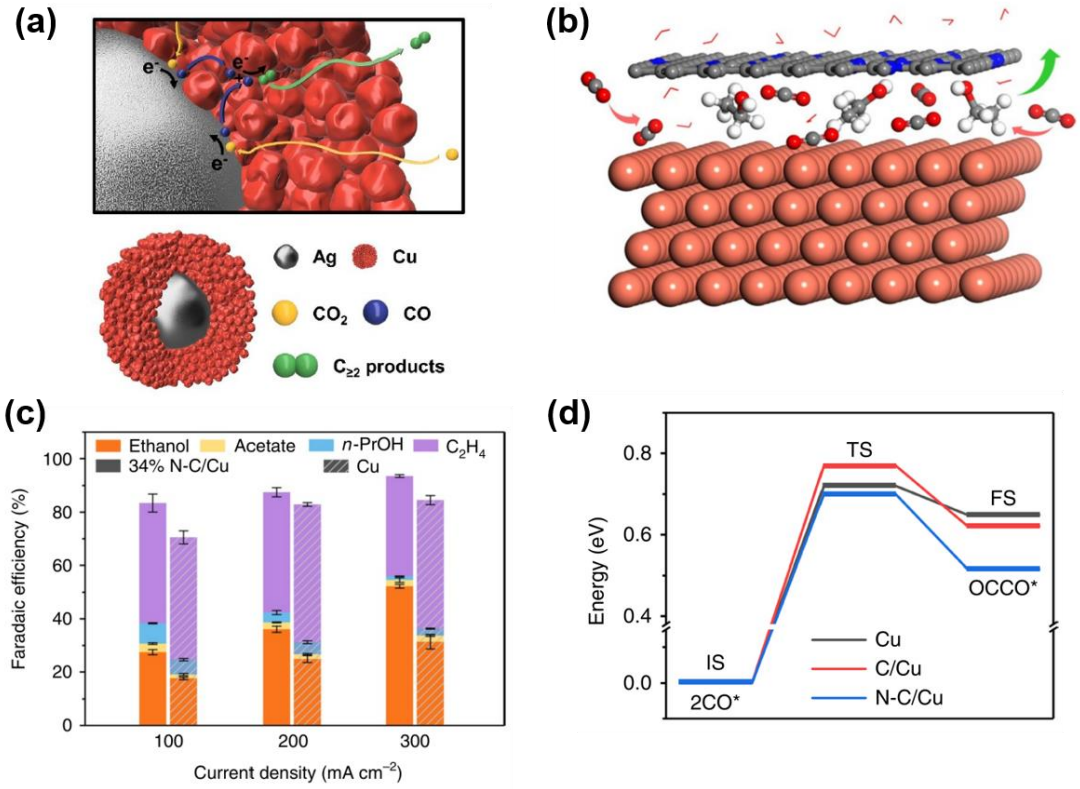

Figure 7. (a) ECR reaction mechanism on an Ag-Cu nanozyme. Reprinted from O'Mara et al.[166], with permission. Copyright 2019 American Chemical Society. (b) Illustration of CO_2 intercalation into the interface of confined Cu electrode (N-C/Cu) to form C_2H_5OH. (c) C_{2+} FEs on bare Cu and 34% N-C/Cu under varied current densities. (d) CO dimerization energy diagrams of the initial states (ISs), transition states (TSs), and final states (FSs) on different catalysts. Reprinted from O'Mara et al. [30], with permission. Copyright 2020 Nature.

3.1.4. Exposed Crystal Facet

Rational regulation of crystal facets to exhibit favorable atomic structure and coordination provides an effective strategy for maximizing the exposure of active sites and thus enhancing the electrocatalytic activity. The exposed crystal facets can also influence the adsorption of electrolytes on the catalyst surface, thus affecting the catalytic performance. For example, for strongly adsorbing electrolytes such as sulfuric acid, the strong adsorption of sulfate anions on to the (111) facets of single-crystal Pt can block the active sites and lower the catalytic activity. In addition to electrolytes, different exposed crystal facets can

preferentially absorb different intermediates, which can affect the electrocatalytic selectivity.

As with particle sizes, the crystal facets also have a key role for Cu-based catalysts in the selectivity and activity of ECR. However, the cause of it is not fully understood. Based on existing reports, the activity of C–C coupling on Cu(100) is higher than Cu(111), with Cu(100) increasing the selectivity for C_2H_4 while Cu(111) and higher index planes favor CH_4 as the main gaseous product. Compared to a polycrystalline Cu surface, a single crystalline Cu(100) surface showed higher activity to C_2H_4 production, and nanostructured Cu catalysts possess better selectivity for C_2 production due to higher exposure of Cu(100) facets. Huang et al. used DFT calculations and showed that Cu(100) can achieve a high CO* coverage and lead preferentially to the low-overpotential CO* dimerization pathway for C_2H_4 [167]. Huang and co-workers synthesized various Cu_2O nanoparticles (NPs) [168], which included c-Cu_2O NPs with (100) facets, o-Cu_2O NPs with (111) facets, and t-Cu_2O NPs with both (111) and (100) facets, and measured the selectivity of ECR to C_2H_4. The authors carried out DFT calculations and discovered that CO tended to be adsorbed on the Cu_2O(100) facets and the joint interface between (100) and (111) facets. This supports the experimental results showing that the t-Cu_2O NPs have the highest selectivity among the three samples. Further, the Fermi level of Cu_2O is lower on the (111) than on the (100) facets (Fig. 8), which facilitates the charge transfer between Cu_2O(111) and (100) facets, promoting the kinetics for the whole reaction.

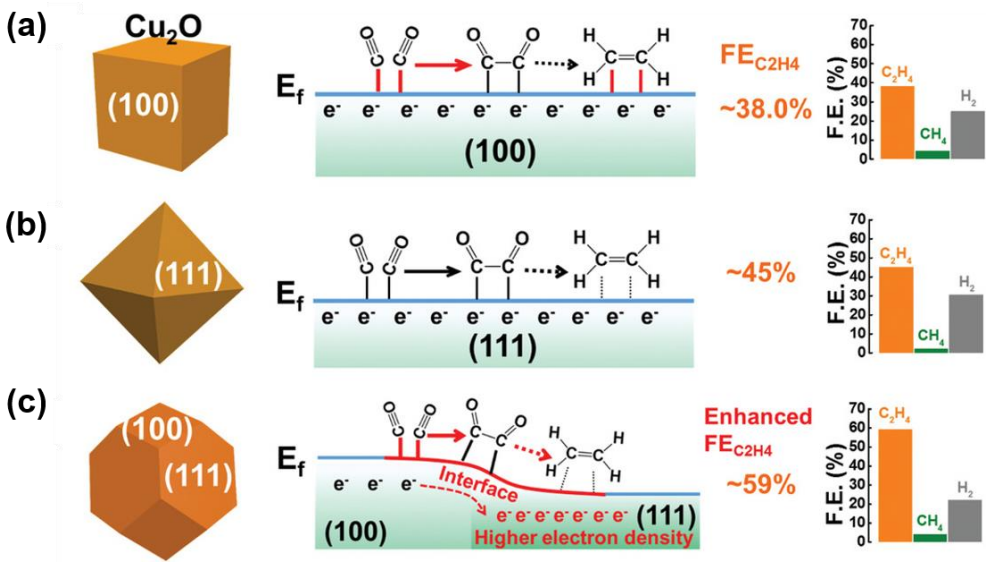

Figure 8. Formation of C_2H_4 on the (a) (100) facets of c-Cu_2O, (b) (111) facets of o-Cu_2O, and (c) (100) and (111) facets of t-Cu_2O. Reprinted from Gao et al. [168] with permission. Copyright 2020 Wiley-VCH GmbH, Weinheim.

3.1.5. Surface Oxidation State

In addition to morphological features, recent studies have shown that the oxidation state of the copper species strongly influences the formation of C_{2+} products [169-171]. In fact, the reduction reaction of copper oxide is thermodynamically and kinetically more favorable than that of ECR, so it is inferred that the reduction of copper oxides takes place before the generation of C_{2+} products [103]. Indeed, several studies have shown that metallic copper is the only active site during the ECR [172, 173]. However, other studies found that some metastable thin Cu_2O layer could be retained after the process of ECR, giving rise to more C_{2+} products through orbital overlapping between oxygen from copper and CO_2 molecules [174]. Theoretical calculations showed that the thermodynamics and kinetics of the CO_2 reduction and CO dimerization reactions were significantly enhanced due to the presence of subsurface oxygen [175]. In situ experimental techniques are required in order to determine the oxygen content in the copper electrode prior to their quick reoxidation. Among them, selective oxygen plasma is a scalable and controllable technique to reconstruct and activate the surface of a copper electrode without high temperature sintering

[87].

Mistry et al. used oxygen and hydrogen-based plasma to modulate the chemical environment of polycrystalline Cu and constructed a new oxidation layer [87]. Through operando XPS and scanning transmission electron microscopy (STEM), they gained insights into the changes of the Cu^+ species and oxidative Cu surface during the process of ECR. STEM elemental mapping by energy dispersive X-ray spectroscopy (EDS) showed that the plasma-activated surface of Cu electrodes was significantly reduced and porous structures appeared during the ECR (Fig. 9). After treatment with an oxygen plasma, a thin oxide film formed over the metallic Cu film, with an inner layer of Cu_2O and an upper layer of CuO, respectively. Some CuO over the single-layer consisting of oxygen atoms was found, and rich Cu^+ sites could remain stable in the reaction. The Cu electrode that was treated in an oxygen plasma achieved a C_2H_4 FE of 60%, in contrast, the H-plasma treated samples showed poorer activity for C_2H_4 formation.

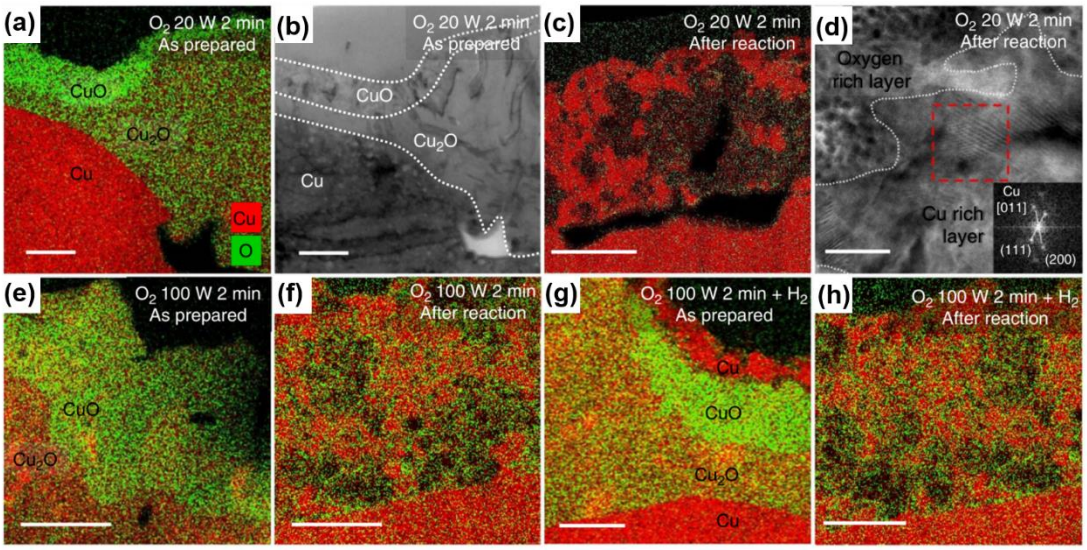

Figure 9. EDS elemental maps of Cu foil treated under various plasma conditions. Scale bars: (a–c) 300 nm, (d) 20 nm, and (e–h) 200 nm. Reprinted from Mistry et al. [87] with permission. Copyright 2020 Nature.

3.1.6. Vacancy or Defect

An effective approach to further optimize the catalytic performance in electrocatalysts is creating surface defects. Vacancies represent a lattice position that is unoccupied because the atom is missing [176]. Oxygen vacancies [177-179], nitrogen vacancies [180], sulfur vacancies [181], and carbon vacancies have been reported to act as active sites [182-184]. The introduction of vacancies can favorably alter the electronic structure of the catalyst, improving charge transfer and providing optimal adsorption energetics for the intermediates of the electrocatalytic reactions.

A major bottleneck of the CO_2 reduction reaction lies in the concurrent HER due to both possessing a similar equilibrium potential range. As catalytic selectivity is related to intrinsic electronic structure, we can take advantage of vacancies or defects to alter or tune the electronic structure. As a typical study, Zhuang et al. developed a vacancy-rich Cu_2S-Cu-V core–shell nanoparticle catalyst that could efficiently catalyze ECR to *n*-C_3H_7OH and C_2H_5OH (Fig. 10) [29]. Theoretical calculations showed that subsurface S atoms and surface Cu vacancies could guide the pathway of reaction to the C_2H_5OH by suppressing C_2H_4 generation. Reaction results confirmed this conclusion in an H cell system, where the Cu_2S-Cu-V achieved a C_2H_5OH FE of 23% at −0.95 V (*vs*. RHE). It is worth noting that the ratio of C_2H_5OH to C_2H_4 on Cu_2S-Cu-V is almost six times that found with bare Cu nanoparticles.

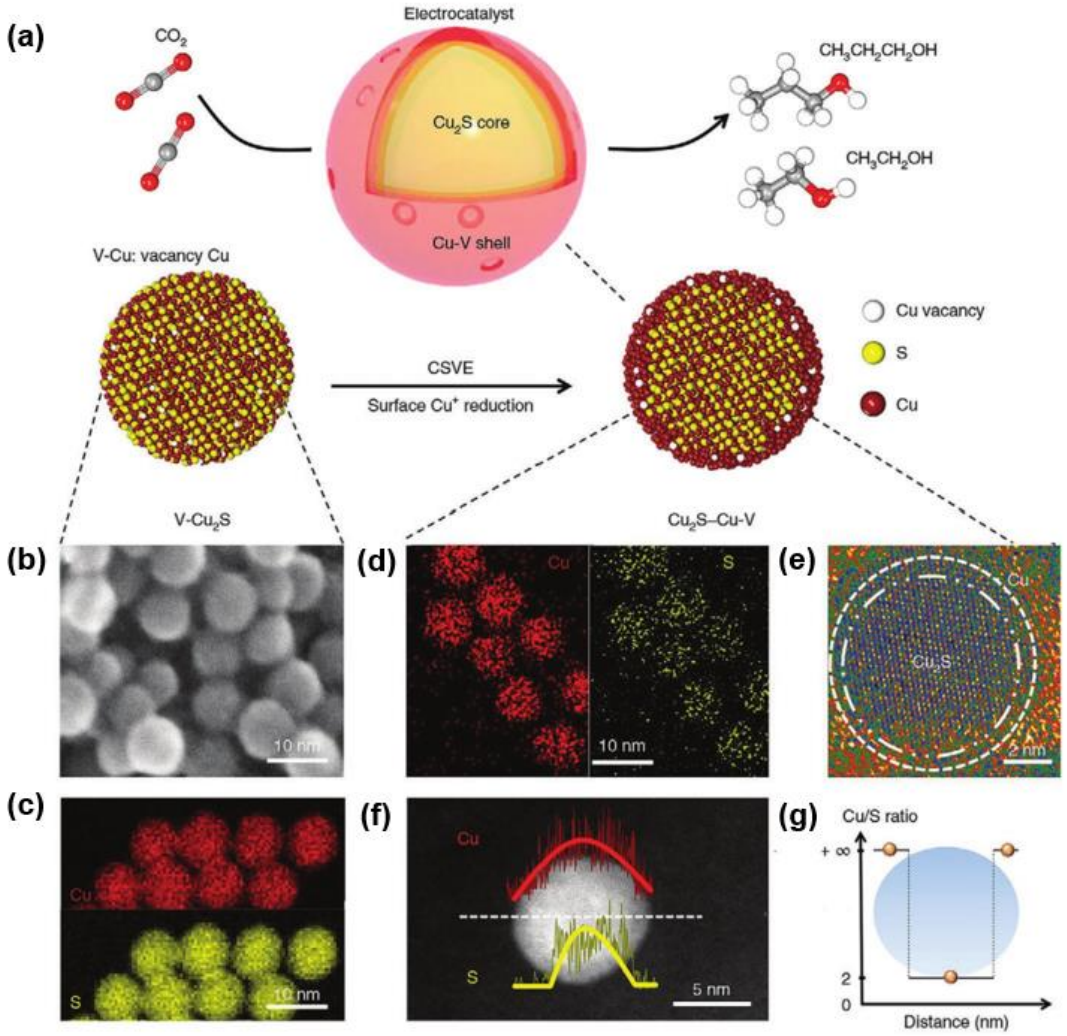

Figure 10. Control of the defects of Cu-based catalysts to tune the ECR activity. (a) Schematic illustration of the design of Cu_2S-Cu-V (V denotes vacancy) core-shell-vacancy engineered (CSVE) catalyst. (b) TEM image and (c) EDS maps of the original V-Cu_2S. (d) EDS maps, (e) high-resolution TEM image, (f) EDS line scanning profiles, and (g) Cu/S atomic ratio distribution of Cu_2S-Cu-V. Reprinted from Zhuang et al. [29] with permission. Copyright 2018 Nature.

3.1.7. Porosity

Generally speaking, the pore size, pore volume, and interconnected hierarchical pore structure, composed of a combination of macropores, mesopores, or micropores, largely determines the accessibility and enrichment of reactants to active sites (e.g., O_2, CO_2, and N_2) and the diffusion dynamics of the electrolyte [185–187]. A porous structure is expected to facilitate the diffusion of

CO_2, reaction intermediates, and reduction products during the ECR. Also, it allows for exposure of more active sites of a catalyst, enabling an effective contact with the working electrode surface, thereby forming a large density of three-phase contact points between CO_2, electrolyte, and catalyst, which is favorable for a more efficient ECR. As an example, Bell et al. utilized a standard dealloying process of CuAl particles to induce an intra-particle nanoporosity [188]. The specific surface area of Cu hollow fibers increased from 0.126 $m^2 g^{-1}$ to 6.194 $m^2 g^{-1}$, leading to a drastically increased performance with high current densities at low overpotentials for ECR.

3.2. Doping

Chemical doping with heteroatoms is an effective strategy to boost electrocatalytic activity [23, 189, 190]. Dopant impurities mean that foreign atoms are placed into the lattice of a host material [191]. The introduction of heteroatoms can not only change the surface electronic structure, but it may also modify the adsorption favorability of reactants and intermediates. Heteroatom doping can be considered for the cases of either non-metal-atom doping or metal-atom doping. In the case of non-metal-atom doping, nitrogen, sulfur, oxygen, boron, and phosphorus atoms are usually selected as heteroatoms to modify the electrocatalytic performance of pristine materials. Specifically, the incorporation of non-metal atoms can tune the bandgap of a catalyst, resulting in an enriched charge density and higher intrinsic conductivity. It also decreases the binding energies of reactants, leading to a lower onset overpotential required to drive the electrocatalytic process. Likewise, doping with foreign metal atoms can be used to tailor the electronic structures and optimize the absorption free energy of intermediates in order to improve the electrocatalytic activity.

Recently, doping of Cu-based materials for electrochemical CO_2 reduction to C_2 products has attracted increasing attention. It has been reported that doping is correlated with selectivity and stability for CO_2 reduction, which is mainly attributed to the electronic configuration of the surrounding atoms. For instance,

Zhou et al. used boron as a dopant to tune the ratio of $Cu^{\delta+}$ to Cu^0 active sites and the average oxidation state of the copper. The author further investigated the relationship between the copper oxidation state and the total C_2 FE, and obtained a volcano plot that peaks with an impressive FE of 79 ± 2% at an average copper valence of +0.35 [192].

Recently, Wang and co-workers developed a fluorine-modified copper catalyst [147], and improved the selectivity and yield of C_{2+} production during the ECR. Fluorine was claimed to promote water activation, CO adsorption and hydrogenation of *CO to *CHO that can readily undergo a subsequent coupling. X-Cu (where X = F, Cl, Br or I) catalysts were further synthesized using a solvothermal method followed by electroreduction. The CO adsorption capacity was found to decrease in the sequence of F-Cu > Cl-Cu > Br-Cu > I-Cu, which was ascribed to the concomitant increase in the percentage of Cu^+ sites with the increasing electronegativity of halogen in the X-Cu catalysts, since the Cu^+ site can enhance CO adsorption. Moreover, the authors used D_2O as a solvent in 1 M KOH and measured the kinetic isotopic effect (KIE) of H/D, discovering that the KIE over the F-Cu catalyst was close to 1. This supports that F^- on copper accelerated H_2O activation.

Besides boron and fluorine, hydroxides and oxides have also been employed as dopants to tune the adsorbed hydrogen on Cu [23]. It was found that C_2H_5OH was the main C_2 product attained, with a FE of 43% and a partial current density of 128 mA cm^{-2} for CO_2 reduction on $Ce(OH)_x$-doped-Cu.

3.3. Alloying

Alloy catalysts allow a synergistic effect through tuning the binding energy of intermediates, such as *H, *CO, *OCHO (bound to the surface through O), *COOH (bound to the surface through C), *CHO, or *COH, for catalytic CO_2 reduction reactions. To date, Cu-based alloys are the only discovered catalysts that can generate C_{2+} products as a major product. Enhanced ECR has been observed on a variety of Cu-based alloys, such as CO on CuAu [193, 194], CH_4 on

CuPd [195], and C_2H_5OH on CuZn [98], etc. Ma et al. synthesized a range of bimetallic Cu-Pd catalysts with ordered, disordered, and phase-separated atomic arrangements, and found that the yield of C_2 products increased with the increase of Cu content following the trend Pd < $CuPd_3$ < CuPd < Cu_3Pd < Cu. This was due to the possibility that the dimerization of *CO may be preferred on the sites with neighboring Cu atoms to form C_2 chemicals (Fig. 11) [153]. Unlike the introduction of other metallic elements into pure Cu-based materials, the de-alloying approach applied to Cu-based alloys (e.g., CuAl and CuZn) allows selective leaching of specific elements to achieve surface atomic rearrangement, thereby modulating the catalytic performance. Among them, acid or alkali treatments are commonly used to remove non-Cu elements from Cu-based alloys. For example, Zhong et al. used a de-alloying method, guided by DFT calculations combined with machine learning, to screen and optimize the alloy catalysts [28]. The volcano plots of CO_2 reduction activity and selectivity were calculated based on the adsorption energy of different metals/alloys for CO and H (Fig. 12a and b). The Cu-Al alloy was found to have excellent catalytic ECR activity to C_2H_4. Subsequently, the Cu-Al catalyst was de-alloyed. The de-alloyed Cu-Al catalyst demonstrated a larger FE for C_2H_4 than that on Cu and nanoporous Cu. Impressively, the de-alloyed Cu-Al catalyst maintained about 85−90% FE for the C_{2+} product at a current density of 600 mA cm^{-2}, and the energy efficiency of C_2H_4 reached up to 34% on the cathodic side (Fig. 12c and d). Mechanistic analysis indicated that the de-alloyed Cu-Al catalyst can provide more active sites with a unique Cu coordination environment, which facilitates the coupling of surface adsorbed *CO.

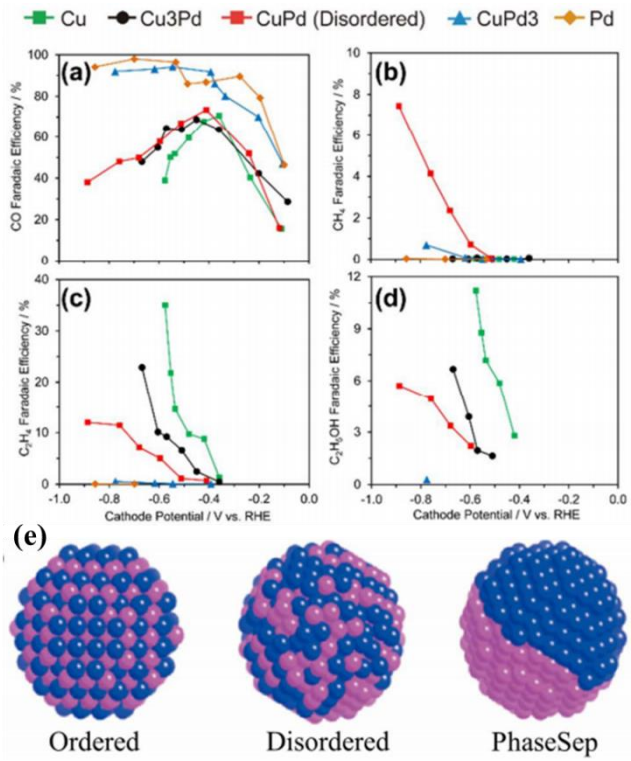

Figure 11. ECR FEs of (a) CO, (b) CH_4, (c) C_2H_4, and (d) C_2H_5OH on ordered, disordered, and phase-separated Cu-Pd. Reprinted from Sadakiyo et al. [153] with permission. Copyright 2017 American Chemical Society.

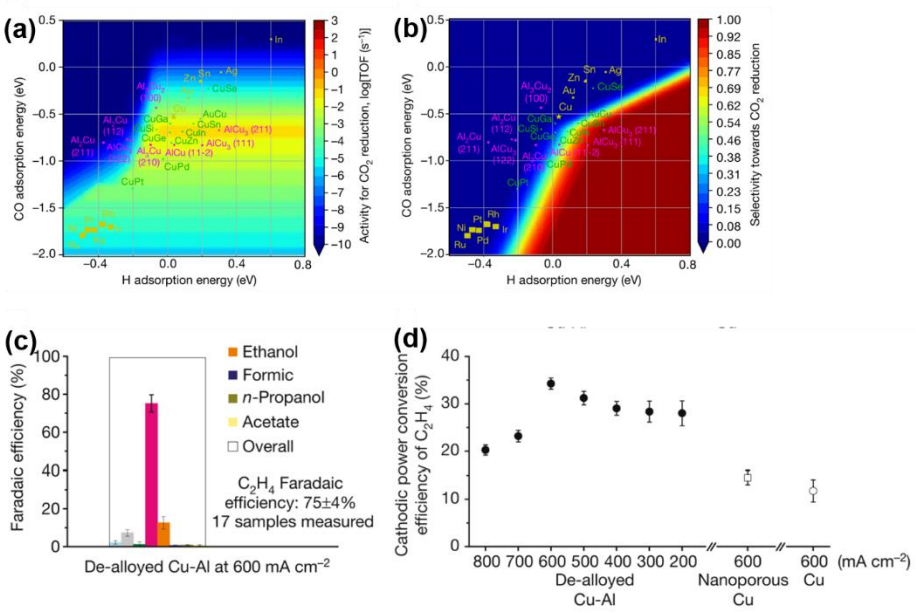

Figure 12. Screening of Cu-based materials based on computational modeling. Two-dimensional (a) activity and (b) selectivity volcano plots for the ECR. TOF represents turnover frequency. Yellow, green, and magenta data points

correspond to average adsorption energies of monometallics copper alloys, and average and low-coverage adsorption energies of Cu-Al surfaces. (c) ECR FE at 600 mA cm^{-2} with 17 de-alloyed Cu-Al samples tested. (d) Half-cell CO_2-to-C_2H_4 power conversion efficiency of different Cu catalysts at varied current densities. Reprinted from Zhong et al. [28] with permission. Copyright 2020 Nature.

3.4. Surface Modification

Surface modification of Cu-based catalysts with some additives and cofactors, such as organic molecules and inorganic nanomaterials, can modulate the catalytic performance of ECR. For example, hierarchically structured Cu dendrites were treated by 1-octadecanethiol so as to generate a superhydrophobic surface that can promote CO_2 reduction on a Cu surface [196]. A triple-phase boundary at the electrolyte-electrode interface was formed (Fig. 13). The Cu dendrites contain wettable and hydrophobic areas that can react with H^+ or CO_2 to form Cu–H* or Cu–COOH* intermediates, respectively. As for the wettable dendrites, H_2 formation was promoted by a higher proportion of Cu–H* groups in aqueous H^+/CO_2 substrates. The formed triple-phase boundary at the electrolyte-electrode interface can facilitate C–C coupling and increase the C_2 production efficiency, due to the surface concentration of Cu-COOH*, and the subsequently formed Cu–CO*, drastically increasing. Compared to an unmodified hydrophilic equivalent, the HER on this superhydrophobic surface was substantially lowered in CO_2-saturated electrolyte, decreasing the FE of 71% to 10%, whereas the CO_2 reduction increased from a FE of 24% to 86%. The hydrophobic electrode attained a FE of 56% toward C_2H_4 and 17% for C_2H_5OH at neutral pH.

Metal hydroxide doping has also proved to be effective, and is widely used in alkaline H_2 evolution and alcohol oxidation reactions [197, 198]. Metal hydroxides offer binding sites for surface *OH, facilitating the breaking of the H−OH bond, and the resulting H is captured by active sites and further involved in the reaction. Luo et al. demonstrated the beneficial effect of this modification for ECR by

synthesizing Cu/metal hydroxide composite catalysts [23]. The $Ce(OH)_x$-doped Cu catalyst was found to achieve a C_2H_5OH FE of 43% (Fig. 14). DFT calculations showed that the metal hydroxides accelerated the dissociation of water and altered the binding energy of H* on the Cu surface. And the adsorbed H* hydrogenates the *HCCOH intermediate, which is more favorable for the formation of C_2H_5OH [208]. Among different metal hydroxides, $Ti(OH)_x$-doped Cu afforded the highest C_2H_5OH-to-C_2H_4 ratio.

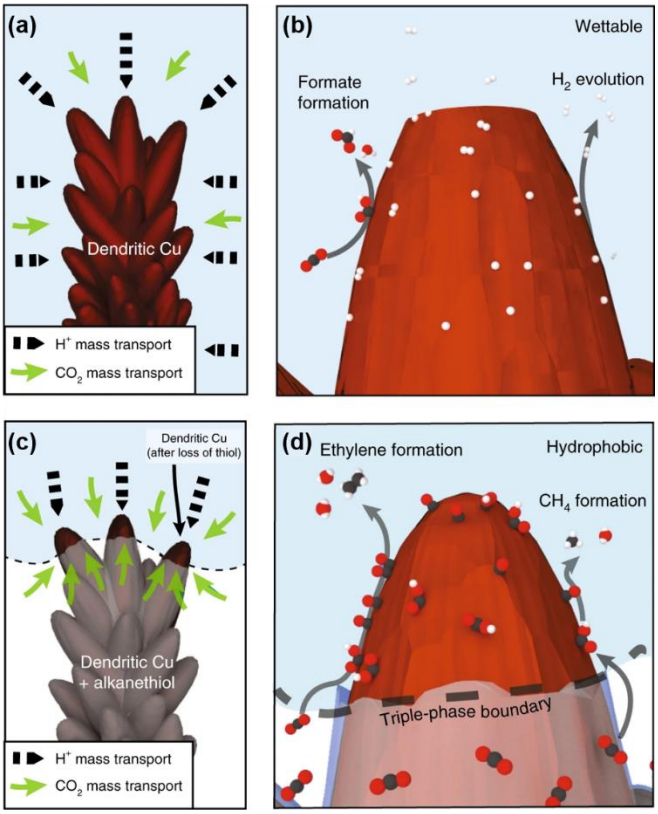

Figure 13. Depictions of (a, b) the wettable dendrite under operation and (c, d) the operation of the hydrophobic dendrite. Reprinted from Wakerley et al.[196] with permission. Copyright 2019 Nature.

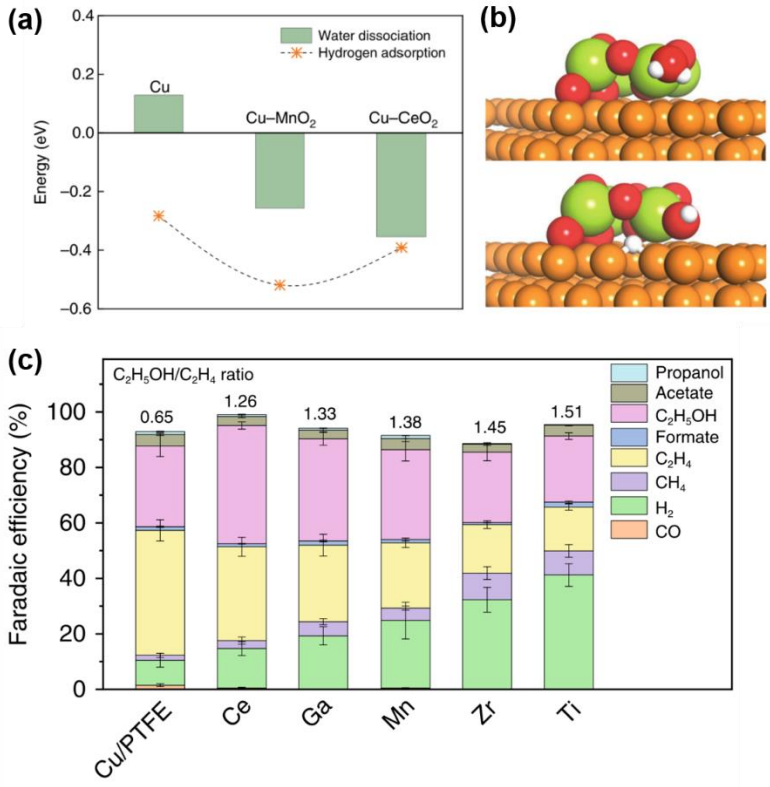

Figure 14. (a) Calculated energies of H_2O dissociation reaction and H adsorption on Cu, Cu-MnO_2, and Cu-CeO_2. (b) Surface configurations of CeO_2/Cu with and without *H. (c) Distribution of ECR products on various hydroxide/oxide modified Cu/PTFE, along with respective C_2H_5OH/C_2H_4 ratio. Reprinted from Luo et al. [23] with permission. Copyright 2019 Nature.

3.5. Support Effect

By loading a catalyst on an appropriate support, its catalytic behavior can be altered according to the type of the support used. There are three different types of support materials that are used; carbon, metal oxide, and polymer. The interactions between Cu and the supporting material can lead to synergistic effects that increase CO_2 adsorption and stability of key intermediates, influencing the final physicochemical properties of Cu-based catalysts.

Carbon materials consist of activated carbon, carbon nanotubes, graphene, graphite, and N-doped graphene, etc. They are the most popular supporting materials due to their low cost relative to the precious metal catalysts, along with their high conductivity, large surface area, and outstanding chemical stability.

Recently, Kim et al. designed hybrid catalysts composed of highly dispersed Cu NPs supported on N-doped porous carbon materials (Cu/NPC), which can serve as cocatalysts (Fig. 15a and b) [121]. By introducing NPC materials with different pyridinic N contents (Cu/NPC-700, Cu/NPC-800, Cu/NPC-900), the selectivity for C_2H_5OH or C_3H_7OH was tuned. It was suggested that the addition of NPC not only affected the size and electronic structure of Cu, but also promoted the adsorption of CO_2 as well as CO production according to theoretical and experimental results. The production of multicarbon alcohols was maximized for the Cu/NPC-800 hybrid catalyst with 20 wt% Cu loading at −1.05 V (*vs.* RHE), achieving a total FE of 73.3% for C_2H_5OH and C_3H_7OH. They further proposed a two-site mechanism with pyridinic N as a CO-producing site and Cu nanoparticles as a catalytic site. Taking advantage of the synergy between catalyst and carrier, Quan et al. synthesized oxide-derived Cu/carbon (OD Cu/C) catalysts through carbonization of a Cu-based metal organic framework (MOF) (HKUST-1) [95]. The resulting materials exhibited a high selectivity for ECR to alcohol compounds with the total FE of 45.2~71.2% at –0.1 to –0.7 V (*vs* RHE). The significant improvement in the activity and selectivity of OD Cu/C toward alcohol generation was speculated to be associated with the collaborative effect between the highly dispersed copper and the porous carbon matrix. In addition, the resulting porous structure reduced the diffusion resistance for overall mass transfer, which is conducive to the rapid movement of CO_2 and alcohol species.

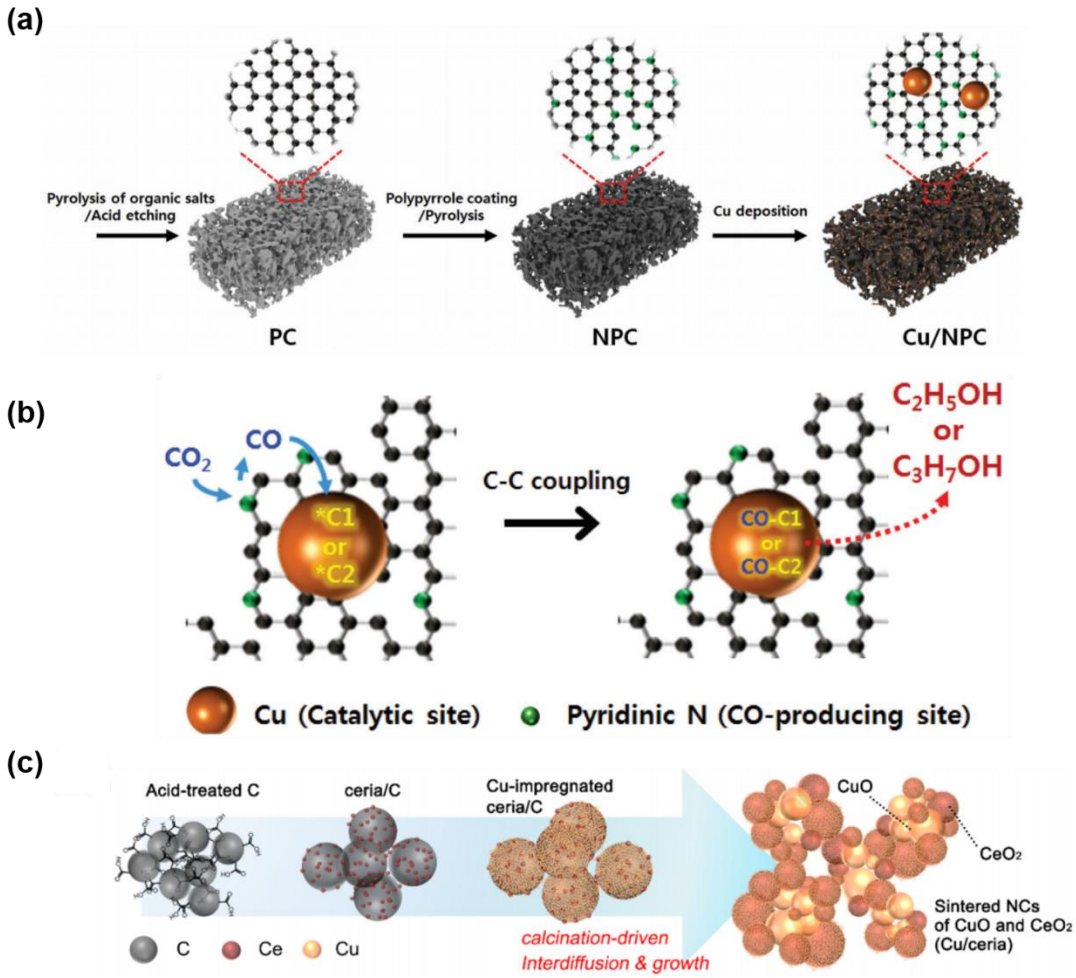

Figure 15. (a) Schematic of the synthesis of Cu/NPC. (b) Two-site mechanism involving the pyridinic N CO-producing site and Cu catalytic site on Cu/NPC. Reprinted from Han et al. [121] with permission. Copyright 2020 Royal Society of Chemistry. (c) Schematic of the synthetic of Cu/ CeO_2. Reprinted from Lee et al. [200] with permission. Copyright 2019 American Chemical Society.

Although carbon supports have many advantages, trace metal impurities such as Cu in carbon supports can dramatically alter ECR catalytic activity, which should not be neglected. This is particularly a consideration with graphene oxide. Therefore, special care has to be paid not to mislead on the origin of ECR activity when carbon-based materials are employed as support materials for electrocatalysts. Before employing them as the support material, pre-washing them in ultrapure nitric acid is highly recommended to decrease effects by metallic impurities.

The support interaction between metal and oxide has been extensively utilized to control the reactivity in catalysis. Meanwhile, the interaction of metal oxide support with Cu may help to stabilize the electronic interaction, NP size and morphology, and oxygen spillover during the catalysis reaction. Copper-ceria (Cu-CeO_2) metal-oxide interfaces that act as an active site for C–C coupling were proposed for selective electrochemical C–C coupling reactions by Hwang and coworkers [200]. By the impregnation of a copper precursor into hydrothermally prepared CeO_2/C and subsequent calcination at 400 °C in air, Cu/CeO_2 catalysts with a high density of interfaces were synthesized (Fig. 15c). Therefore, the Cu–CeO_2 interface was constructed by sintering sub-10 nm crystals to maximize interfacial density and synergistic interaction at the interface. The authors conducted DFT calculations and observed that the dimerized *OCCO intermediate can be stabilized by interfacial active sites, with an aim of promoting the reaction pathway specific to the C–C coupling reaction. Meanwhile, the HER was suppressed. In comparison with control Cu catalysts, by constructing the interface with CeO_2, HER selectivity was reduced from 40.0% to 14.6%, whereas the FE of C_2H_4 and C_2H_5OH production increased from 38.8% to 64.7%. The atomic distribution and domain formation of Cu can be influenced by the surrounding CeO_2 support, which affects the C–C coupling activity.

Materials based on graphitic carbon nitride (*g*-C_3N_4), the most stable phase among all the allotropes of carbon nitride, have attracted much attention. An electrocatalyst of tetrahedral (T_d) copper clusters supported on *g*-C_3N_4 (T_d-Cu_4@*g*-C_3N_4) was designed by Wang et al. to promote high selectivity conversion of CO_2 to C_2H_5OH at low potential. [201] They found a tetrahedral Cu_4 cluster was firmly anchored on the hole of the *g*-C_3N_4 substrate owing to the strong interaction between the Cu_4 cluster and the natural holey structure of *g*-C_3N_4. Each Cu atom at the bottom (Cu_b) interacts with two twofold-coordinated N atoms, while the Cu atom at the top (Cu_t) bonds to three Cu atoms at the bottom (Fig. 16). According to electronic and thermodynamic analysis, the metallic Cu

site has a stronger affinity toward the capture of CO_2 molecules and to further reduce to *CO, while the existence of a Cu_b^{x+} site promotes an increase to the local CO concentration. The synergistic effect of Cu_t^0 and Cu_b^{x+} atoms effectively reduce the limiting potential for the *CO reduction into *CHO step. Surprisingly, the C–C coupling reaction is obtained by two *CHO species with a low kinetic barrier of 0.57 eV on the Cu_t^0-Cu_b^{x+} atomic interface. Subsequently, C_2 intermediates prefer to form sp^3 hybrid C atoms, leading to the release of C_2H_5OH product at a low potential (0.68 V).

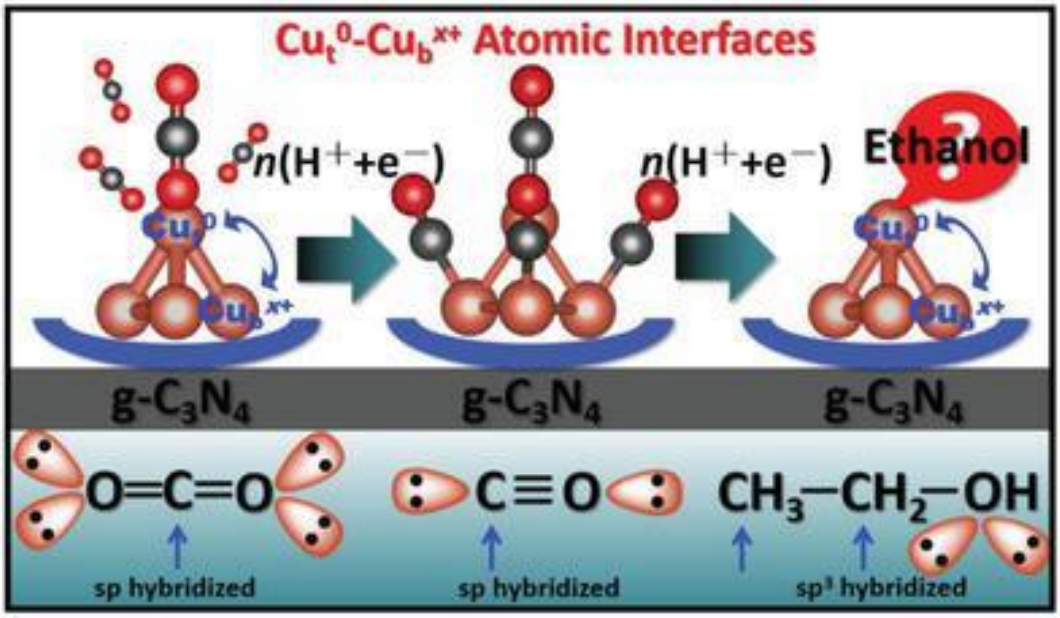

Figure 16. Simplified schematic of reaction mechanism for ECR into CH_3CH_2OH on T_d-Cu_4@*g*-C_3N_4 and hybrid orbital analysis of carbon atom in CO_2, CO, and CH_3CH_2OH. Reprinted from Bai et al. [201] with permission. Copyright 2019 Wiley-VCH GmbH, Weinheim.

3.6. Interface Engineering

In a heterogeneous catalysis process, the interactions at the interface between two different materials result in simultaneous changes to their electronic states and chemical properties. In order to better understand the interface reaction and the high surface sensitivity, free mass transport, and insusceptibility to gas evolution, in situ attenuated total reflection infrared spectroscopy has been successfully adopted to study the electrochemical interface of ECR. Interface

engineering has been widely applied to improve the catalytic activity of nanomaterials because the interface can play a dominant role in altering the binding, transformation and transport of surface species such as intermediates, electrons, and adsorbents between different domains.

Cui and co-workers chose N-doped nanodiamond (N-ND) that contains a dominant N-sp^3 C component as a support to construct a (N-ND)/Cu interface [32]. They synthesized N-ND films by carrying out microwave plasma-enhanced chemical vapor deposition on a nanodiamond seed on a pre-functionalized silicon wafer substrate, and further sputtering of Cu onto the as-prepared N-ND film results in the desired N-ND/Cu composite (Fig. 17). The catalyst exhibits a FE of ~63% towards C_2 oxygenates (the $FE_{CH3COOH}$ of 34.7% and $FE_{CH3CH2OH}$ of 28.9%) at applied potentials of only –0.5 V (*vs.* RHE). Moreover, this catalyst shows an unprecedented persistent catalytic performance up to 120 h, with steady current and only 19% activity decay. DFT show that CO binding is strengthened at the copper/nanodiamond interface, suppressing CO desorption and promoting C_2 production by lowering the apparent barrier for CO dimerization.

A heterostructure with abundant interfaces allows for the tuning of the catalytic performance by interface engineering. For example, a designed copper oxide/hollow tin dioxide heterostructure catalyst [202] can tune the products from CO to HCOOH at high faradaic efficiency by changing the electrolysis potentials from –0.7 V to –1.0 V (*vs.* RHE). Constructing bifunctional electrocatalysts from heterogeneous nanostructures (i.e., heterostructures) is a promising approach, as they can yield synergistically enhanced kinetics relative to their single components due to the increase of active sites and electron redistribution at their interfaces..

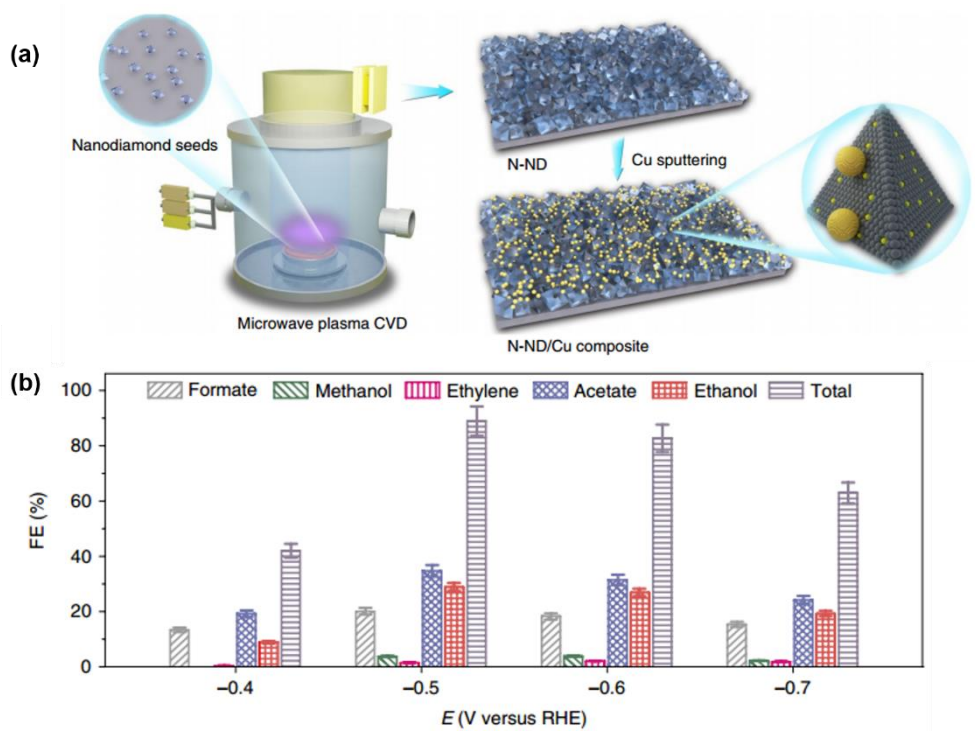

Figure 17. (a) Schematic of the preparation of N-ND/Cu composite. (b) Total ECR FE and FEs toward different products on N-ND/Cu. Reprinted from Wang et al. [32] with permission. Copyright 2020 Nature.

4. Role of Electrolyte to Promote C_{2+} Evolution

It has been well acknowledged that the electrolyte plays a unique role in the ECR reaction, which not only is indispensable as the reaction media in most cases, but also greatly influences the solubility and activation of CO_2, stabilization of intermediates, reaction activity, product selectivity and so on. The evolution of C_{2+} products can be tuned by finely designing the electrolytes, including their pH, selecting different cations and anions, as well as changing the solvent type.

4.1. pH Effect

There have been both experimental and theoretical studies that have demonstrated the dependence on pH to produce C_{2+} products from ECR. Using a microkinetic model, Chan et al. [203] investigated the effects of pH on the activities and selectivities of C_1 and C_2 products. It was found that with water as the proton source, the rate-determining proton-electron transfer steps for C_1 and

C_2 products were different, thus resulting in a distinct dependence on pH. Between pH 7 and 13, the overpotential for C_2 products shifted more than that for C_1 products, which led to enhanced activity and selectivity of C_2 products under alkaline conditions.

Although it has been suggested that alkaline electrolytes might be beneficial for C_{2+} products, experimental study of the direct effect of hydroxide ions on the ECR performance has proven challenging, because at higher pH in aqueous solutions CO_2 reacts to form carbonates upon its dissolution. To overcome this, Sargent et al. [156] harnessed flow cells with gas diffusion electrodes, in which the gas diffusion layer allowed for the access of CO_2 to the catalyst surface and the occurrence of ECR before the formation of carbonates. In this flow cell configuration, the local concentration of CO_2 was substantially increased and the direct effects of hydroxide ions were able to be clarified. In an alkaline electrolyte of 7 M KOH, the FE of C_2H_4 reached 70% with a Cu catalyst at −0.55 V (*vs.* RHE). From the experimental and characterization results, it was suggested that the hydroxide ions from the high concentration alkaline solution could promote CO_2 activation and the C–C coupling reaction through their interaction with the Cu catalyst surface, thus decreasing the onset potential for C_2H_4 formation. In another report that also used 7 M KOH as an electrolyte, a C_2H_4 partial current density of 1.3 A cm^{-2} with a cathodic energy efficiency of 45% was achieved, which further confirmed the advantage of alkaline electrolyte for ECR to produce C_2H_4.

4.2. Cation Effect

It has been reported that ECR performance can be influenced by the alkali metal cations of the electrolytes [204]. For example, in the initial work of Hori and Murata [205], the cation size was found to have a strong influence on the selectivity of CO_2 and CO reduction on polycrystalline Cu, in which larger cations preferred the formation of C_{2+} species. There have been different explanations for the mechanism of this cation effect. Hori and Murata ascribed the change in ECR

selectivity with cation size to the difference of the outer Helmholtz plane (OHP) potential, based on Frumkin's theory [206]. The OHP potential will shift to a more positive value with specific cation adsorption on the electrode, and the value increases with cation size due to its lower hydration number. In another theoretical work, it was suggested that specific adsorption of alkali cations was not applicable to the conditions of ECR, in part due to the very negative reduction potentials of alkali ions on transition metal electrodes [207].

In spite of the different views regarding the effects of cations on ECR performance, recently there has been a big step forward on the experimental side of ECR. In the previous section, it was concluded that alkaline solution was beneficial to the ECR and the formation of multicarbon products, partly due to the suppression of the competing HER because of the slow kinetics for water reduction and the lower coverage of adsorbed hydrogen. Typically, in acidic solutions, HER will occur more easily than the ECR reaction. While in the presence of a high concentration of potassium cations in the electrolyte and at the electrode, CO_2 activation could be accelerated for efficient ECR to proceed in strong acidic (pH < 1) solutions [208]. Since the acidic electrolyte can avoid the transformation of CO_2 to carbonate, a single-pass CO_2 utilization of 77% was obtained with a selectivity to multicarbon products (including C_2H_4, CH_3CH_2OH, and *n*-propanol) of 50%. The authors attributed the C_{2+} selectivity to electrostatic interactions of the potassium cation with the electric dipole of specific adsorbates, favoring C_{2+} reaction pathways.

4.3. Anion Effect

The most commonly studied electrolyte in ECR is $KHCO_3$ with HCO_3^- anion owing to the fact that CO_2-(bi) carbonate-water equilibrium helps maintain a neutral bulk pH. Actually, the anions of the electrolytes also have an influence on the performance of ECR to C_{2+} products. Back to as early as 1988, Hori and coworkers investigated ECR on a Cu electrode in various electrolyte solutions, and showed that C_{2+} products such as hydrocarbons and alcohols were preferred

to form in KCl, $KClO_4$, K_2SO_4, and dilute $KHCO_3$ solutions, while K_2HPO_4 solutions favored the HER [209]. The authors explained this phenomenon in terms of a nonequilibrium local region of high pH close to the electrode based on the idea that solutions with high pH were beneficial to the production of these C_{2+} products.

In a recent report, using a CuO electrocatalyst decorated with Bi single atoms and oxygen vacancies, Sun et al. studied the effect of various factors on the FE of C_2H_4 in ECR, among which they found that replacing HCO_3^- with halide anions such as Cl^- and Br^- resulted in an obvious decease in C_2H_4 FE, probably due to the preferred adsorption of halide anions on the Bi-CuO surface compared to that of CO_2 [210]. Increasing the concentration of both K^+ and Cl^-, namely by using a higher concentration of KCl solution, gave a higher C_2H_4 FE than that in $KHCO_3$ solution, which was due to the reaction benefiting from the promotional effect of the K^+, as mentioned in the previous section ("Cation Effects"). Therefore, in the case of practical ECR, the effects of cations, anions, and pH are synergistic and researchers need to consider the combined effects together with the specific electrocatalyst involved.

4.4. Solvent Type

Aqueous solutions are the most commonly used electrolytes for ECR since water is cheap and environmentally friendly. With the design and development of electrocatalysts as well as tuning the previous discussed factors involved in the electrolytes, various products ranging from C_1 to C_3 can be obtained in aqueous electrolytes. Although other kinds of solvents, such as organic solvents and ionic liquids (ILs), have been investigated for ECR due to their merits in CO_2 solubility and suppression of the HER, most of them only exhibited enhancement in affording C_1 products. It is still meaningful to explore other types of solvents for C_{2+} products evolution.

Oxalate is a high value product that can be produced from ECR in organic solvents. From the reported results, it can be summarized that aprotic solvents,

such as *N*,*N*-dimethylformamide, propylene carbonate, acetonitrile (AcN), together with ammonium salts are the common combination for electrolytes for oxalate production from ECR [211-213]. In a recent report by Zhang et al., a new aprotic and basic phosphonium-based IL ([P4444][4-MF-PhO]) was designed and synthesized to improve the performance for ECR to produce oxalate [214]. With 0.5 M [P4444][4-MF-PhO]/AcN as electrolyte on a Pb electrode, an oxalate FE of 93.8% with a partial current density of 12.6 mA cm^{-2} was achieved. Mechanism studies revealed that the ester and phenoxy functional groups in [P4444][4-MF-PhO] can act as double active sites to activate CO_2. Additionally, in the electrolyte with a phosphonium-based ionic environment, the potential barriers for the formation of the key intermediates were lowered, which enhanced the performance of ECR to oxalate.

Recently, Fortunati and coworkers showed that acetate anions (strong Lewis bases) imidazolium-based ILs favor CO_2 capture and H_2 production, whereas fluorinated anions (weaker Lewis bases) are beneficial for CO_2 electroreduction [215]. 1-Butyl-3-methylimidazolium triflate was demonstrated to be a promising IL, displaying a high CO FE (>95%) with good stability for 8 h at large currents from −20 mA to −60 mA. Other possible explanations on enhancement of CO_2 reduction in ILs involve cation hydrogen-bond stabilization of transition species and carbene-tuned coordination of CO_2 through cation complexes [216] A recent work from Gebbie et al. demonstrated the impact of collective ion correlations and self-assembly on ECR reactivity in IL-based electrolytes [217]. Modulation of ionic correlations via concentration enables enhanced electrostatic screening, thus promoting cleavage of bonds and stabilizing the key intermediate $CO_2^{\bullet-}$ via localizing electric field gradients to electrode surfaces. This allows for improvement of potential-dependent CO_2 reduction rates and CO FE at intermediate concentrations of 0.9 M IL in acetonitrile.

5. Other Factors Affecting C_{2+} Formation

In addition to the type of electrolyte, pH, and ion type, the C_{2+} selectivity is

also affected by the purity of CO_2 reactant. Wang et al. investigated the electrochemical reduction of mixed CO_2/CO feeds on CuO_x NPs [218]. The yield of C_2H_4 was substantially enhanced, pointing to the absence of site competition between CO_2 and CO molecules on the reactive surface. Meanwhile, the influence of SO_2 impurity gas in the electrochemical conversion of CO_2 was explored by Jiao and coworkers on three different materials, Ag, Sn, and Cu that are selective catalysts for CO, HCOOH, and C_{2+} products, respectively [219]. They found that the presence of SO_2 impurity decreased the CO_2 conversion efficiency owing to the reduction of SO_2 being thermodynamically more favorable than CO_2. The presence of SO_2 was observed to have no effect on the selectivity of Ag- and Sn-based catalysts, while inhibiting the formation of C_{2+} products on Cu catalyst. Besides, using supercritical CO_2 as a solvent and reactant was shown to enable enhanced catalytic activity and cathodic current density. At the same time, the competitive HER can be suppressed [220].

6. Challenges in CO_2 Reduction to C_{2+} Species on Cu-Based Electrocatalysts

Selective and efficient catalytic conversion of CO_2 into value-added fuels and feedstocks provides an ideal avenue to high-density renewable energy storage. Cu- based electrodes exhibit excellent ECR selectivity toward C_{2+} products. However, identifying the true functional site of Cu electrocatalysts that governs the ECR to C_{2+} products remains a significant challenge due to the fact that the surface state of Cu is dynamic and difficult to predict under working conditions. Furthermore, the stability of Cu electrocatalysts is unsatisfactory, and the deactivation mechanism is not yet fully understood. The following discussion will focus on these two parts in more detail.

6.1. Cu(0) or Cu(I)?

Surveying the literature shows that Cu-based catalysts are the most efficient material for ECR, and Cu is a key component for forming multicarbon products. However, the origin of their outstanding ECR performance is elusive, and the

key oxidation state of Cu is still under debate. The current controversy about the actual active site is whether it is Cu(0) or Cu(I). On the one hand, it was found that Cu NPs, Cu nanocubes and Cu nanoclusters can exhibit a selectivity up to 60% for transformation of ECR to C_{2+} products. Han et al. also found the Cu-based electrodes with mixed oxidation states were all reduced to Cu(0) at the steady stage of ECR, suggesting that the high C_{2+} selectivities are not associated with specific oxidation states of Cu [221]. In addition, an electro-reduction pretreatment was performed on these Cu-based electrodes with mixed oxidation states under harsh conditions to ensure full reduction to Cu(0) before being used for catalyzing ECR. The pre-treated electrodes exhibited a slightly higher selectivity toward C_{2+} products, underpinning the key catalytic role of Cu(0) and the negligible impact of the starting oxidation state of the Cu- based electrodes.

Prior work by Kanan and co-workers demonstrated that the pre-oxidation of Cu can greatly boost its intrinsic catalytic properties toward the formation of C_{2+} products [68]. They attributed this improvement to the remaining active Cu^+ species during the ECR process. Computations conducted by Goddard and co-workers also showed that Cu^+ can work in a synergy with Cu^0 to promote the formation of C_{2+} product by facilitating CO_2 activation and C–C coupling [222]. Unfortunately, the active Cu^+ species are still very prone to being reduced to metallic Cu under ECR conditions, degrading the C–C coupling for C_{2+} product generation. In recent years, several strategies have been used to stabilize the Cu^+ species, including heteroatom doping [109], surface modification [223], and plasma activation [87]. For example, Yu et al. developed a simple spatial confinement approach to stabilize Cu^+ species. They prepared a Cu_2O catalyst with nanocavities, in which in situ formed carbon intermediates covered the local catalyst surface and thereby stabilized Cu^+ species, resulting in a high C_{2+} FE greater than 75%, and a C_{2+} partial current density of up to 267 ± 13 mA cm^{-2} [224].

Despite these advances, operando/in situ characterization techniques should be further developed and employed to gain a deep mechanistic picture of Cu-

based catalysts during ECR.

6.2. Stability of Cu-Based Electrocatalysts

For commercial applications of ECR, the catalyst should provide high performance, i.e., high FE, high current density, and excellent stability for long-term operation. Nevertheless, the stability of the catalysts under ECR conditions has been given considerably less attention in comparison to activity/selectivity issues. Understanding the stability and the deactivation mechanisms of state-of-the-art Cu-based catalysts for ECR will be crucial for developing mitigation strategies to enhance durability.

Nanostructured Cu films have been demonstrated to be excellent ECR catalysts due to their unique features, including high surface area, numerous edge/low-coordinated sites, grain boundaries, and porosity [225, 226]. However, the morphology of the Cu films is prone to change during operation, which profoundly affects the stability of the catalyst. Meanwhile, the complexity of nanostructured catalysts makes it challenging to gain insights into the contribution of each structural feature to the overall improvement in ECR performance. Ren et al. reported that the anodization process of Cu NPs to $Cu(OH)_2$ and Cu_2O, which are then reduced back to Cu(0) nanocrystals (Cu NCs) during ECR (as an in-situ reconstruction event), can improve their selectivity toward *n*-propanol [100]. Cu NCs maintained a remarkable stability in producing *n*-propanol over 12 hours compared to the initial Cu NPs. The authors ascribed this improved behavior to a decreased propensity toward CH_4 formation that can supposedly decompose into graphitic carbon, which then blocks the catalyst surface. By suppressing this route of CH_4 formation, the likelihood of catalyst deactivation via poisoning is also minimized. We note that the poisoning effects of reaction intermediates are still not completely elucidated.

Li et al.[68] fabricated Cu_2O films through annealing of Cu foil in air at different temperatures, followed by electrochemical reduction of the resulting oxide layers. The Cu_2O film showed much better ECR performance in terms of

activity and selectivity toward HCOOH than untreated polycrystalline Cu electrodes (Fig. 18). To determine if there had been any compositional changes to the catalyst during electrolysis, XRD and XPS were performed after operation, and the results showed the Cu_2O layer on the annealed Cu electrode is mostly reduced during ECR. However, they do not completely eliminate the possibility of the presence of a thin metastable Cu_2O layer or other surface-bound Cu^+ species during electrocatalysis. In-depth studies are necessary to elucidate the degradation mechanisms of Cu-based catalysts.

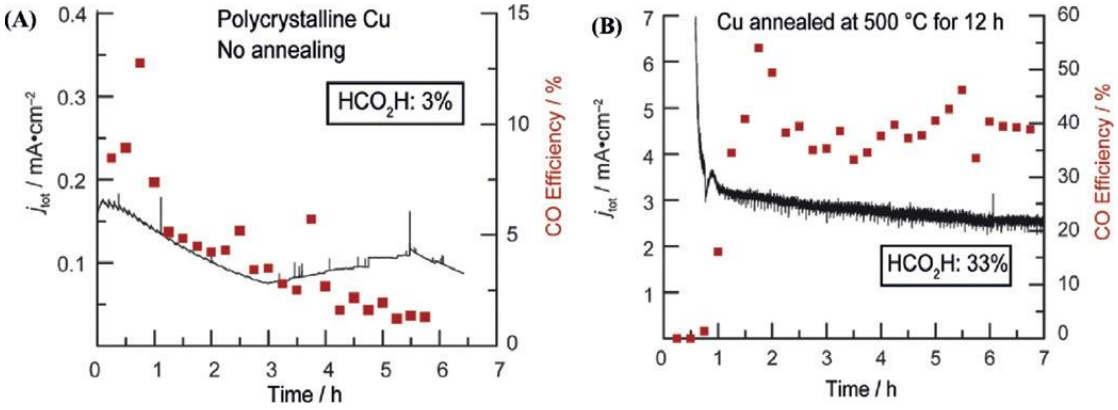

Figure 18. ECR electrolysis data for (a) untreated polycrystalline Cu and (b) Cu_2O film obtained at –0.5 V (*vs.* RHE). Reprinted from Li et al. [68] Copyright 2012 American Chemical Society.

In the pursuit of stabilizing Cu-based catalysts, various strategies have been employed. One approach is to stabilize the morphology to preserve reaction selectivity by confinement. As an example, Li et al. demonstrated that wrapping Cu nanowires with graphene oxide can prevent structural changes and protect the CH_4-selective sites. Another effective strategy to control the shape and size of catalysts is to bind organic stabilizer molecules. Furthermore, pulse electrolysis is recognized as an emerging scheme to stabilize catalysts [227-229].

7. Conclusions and Outlook

ECR has been attracting increasingly more attention in the last few decades as it offers the possibility of producing valuable chemicals and high energy-

density fuels while recycling CO_2 and storing renewable energy. Many intriguing nanoscale structure-activity and structure-selectivity relationships have been discovered to-date. The electrochemical reduction of CO_2 to C_{2+} products has been extensively studied over various electrode surfaces. In this review, we have discussed in detail the mechanisms, the possible reaction paths and the influencing factors of C_{2+} production for Cu-based catalysts. To promote C_{2+} production, the following schemes can be considered:

1) Tandem catalysis, where sequential reactions are coupled and catalyzed by a single nanostructured catalyst with multiple active sites, which presents a number of opportunities to improve chemical transformations. Different catalytic centers can jointly/collaboratively optimize the affinity of the reactant and key intermediates, facilitating coupling of intermediates toward C_{2+} products. It also eliminates the steps for intermediate separation, purification, and transportation, which is especially beneficial in situations where the reaction intermediates (the products of the first reaction) are thermally unstable or toxic.

2) Molecular catalysts containing versatile structures that can be systematically tuned via ligand screening in order to optimize their catalytic performance offers an attractive option to promote selective ECR. Because their active sites are well-defined and uniform, molecular catalysts are also considered as appropriate platforms for gaining mechanistic insights into catalysis.

3) Design and integration of solid electrolytes (such as proton conductors including a porous styrene-divinylbenzene sulfonated copolymer or a caesium-substituted tungstophosphoric acid as well as anionic conductors) enables the production of pure liquid products with high concentrations rather than dilute solutions containing potassium and carbonate residues. A liquid product is easily collected by using a stream of deionized water or a humidified nitrogen flow. This eliminates separation costs. However, the ionic conductivity, electrochemical and mechanical stability of solid electrolytes as well as the quality of the interfacial contacts should be further addressed.

4) Membrane electrode assemblies (MEAs) with a “zero-gap” configuration between a catalyst-coated gas diffusion electrode and an ion-conducting membrane allows high-efficiency CO_2 electrolysis approaching industrial-scale rates. To this end, use of anion-exchange membranes and alkaline anolytes are preferred to inhibit the competitive HER, facilitating yield of C_{2+} products. The degree of K^+ crossover from the anolyte into the cathode through the anion-exchange membrane needs to be considered, which can have a profound influence on the selectivity of Cu catalysts.

In order to bring the ECR process closer to the commercial and applied level, it is necessary to further enhance the catalyst stability, in addition to the activity/selectivity. We have discussed previous studies focusing on the stability of Cu-based catalysts with the aim to highlight this critical issue that has been underestimated so far in the latest literature related to ECR. Possible reasons for catalyst deactivation such as surface reconstruction, contamination, and mechanical failure need to be examined and addressed. Especially, future efforts need to focus on ECR electrolyzer design, such as gas diffusion layers, membranes, solid electrolytes, and interfaces, to accelerate the commercial-grade fabrication of C_{2+} products. A combination of catalytic avenues (e.g., nanostructuring and molecular interface functionalization) developed in an H-cell/flow cell with optimization of MEAs provides a promising way to enhance full electrolyzer energy efficiency and system stability. To efficiently regenerate CO_2 consumed by KOH electrolytes and lower the full reactor voltage, development of bipolar-membrane-based MEAs may offer advantages.

In summary, ECR offers a good opportunity for us to deal with the environmental issues associated with greenhouse gases emitted by human activities, and shows a possibility for achieving clean fuels and chemicals using renewable energy. The combination of advanced in situ/operando characterization techniques and DFT calculations will accelerate the progress of our understanding into the reaction mechanisms, which remains one of the

biggest outstanding challenges in the field. In addition, metrics such as an accurate quantification of energy efficiency, single cycle CO_2 conversion, and product yield rate should be given for comparison and evaluation of ECR toward industrial applications.

Acknowledgements

This work was supported by the National Natural Science Foundation of China (No. 21972010), National Key Research and Development Program of China (No. 2022YFC2105900), and Beijing Natural Science Foundation (No. 2192039).

Conflict of Interest

The authors declare no conflict of interest.

References

1. Liu, Y., Ye, H.Z., Diederichsen, K.M., et al. (2020). Electrochemically mediated carbon dioxide separation with quinone chemistry in salt-concentrated aqueous media. Nat. Commun. ***11***, 2278.

2. Dietzenbacher, E., Cazcarro, I., Arto, I. (2020). Towards a more effective climate policy on international trade. Nat. Commun. ***11***, 1130.

3. Tao, H., Fan, Q., Ma, T., et al. (2020). Two-dimensional materials for energy conversion and storage. Prog. Mater. Sci. ***111***, 100637.

4. Fan, Q., Hou, P., Choi, C., et al. (2020). Activation of Ni particles into single Ni–N atoms for efficient electrochemical reduction of CO_2. Adv. Energy Mater. ***10***, 1903068.

5. Shen, H., Peppel, T., Stunk, J., et al. (2020). Photocatalytic reduction of CO_2 by metal-free-based materials: recent advances and future perspective. Sol. RRL ***4***, 1900546.

6. De Arquer, F.P.G., Dinh, C.-T., Ozden, A., et al. (2020). CO_2 electrolysis to multicarbon products at activities greater than 1 A cm^{-2}. Science ***367***, 661−666.

7. Jia, M., Choi, C., Wu, T.-S., et al. (2018). Carbon-supported Ni nanoparticles for efficient CO_2 electroreduction. Chem. Sci. ***9***, 8775−8780.

8. Li, L., Li, X., Sun, Y., et al. (2022). Rational design of electrocatalytic carbon dioxide reduction for a zero-carbon network. Chem. Soc. Rev. ***51***, 1234−1252.

9. Teeter, T., Rysselberghe, P.V. (1954). Reduction of carbon dioxide on

mercury cathodes. J. Chem. Phys. ***22***, 759−760.

10. Hori, Y., Kikuchi, K., Suzuki, S. (1985). Production of CO and CH_4 in electrochemical reduction of CO_2 at metal electrodes in aqueous hydrogencarbonate solution. Chem. Lett. ***14***, 1695−1698.

11. Ma, T., Fan, Q., Tao, H., et al. (2017). Heterogeneous electrochemical CO_2 reduction using nonmetallic carbon-based catalysts: current status and future challenges. Nanotechnology ***28***, 472001.

12. Weng, Z., Wu, Y., Wang, M., et al. (2018). Active sites of copper-complex catalytic materials for electrochemical carbon dioxide reduction. Nat. Commun. ***9***, 415.

13. Zhang, H., Chang, X., Chen, J.G., et al. (2019). Computational and experimental demonstrations of one-pot tandem catalysis for electrochemical carbon dioxide reduction to methane. Nat. Commun. ***10***, 3340.

14. Gao, S., Lin, Y., Jiao, X., et al. (2016). Partially oxidized atomic cobalt layers for carbon dioxide electroreduction to liquid fuel. Nature ***529***, 68−71.

15. Larrazábal, G.O., Shinagawa, T., Martín, A.J., et al. (2018). Microfabricated electrodes unravel the role of interfaces in multicomponent copper-based CO_2 reduction catalysts. Nat. Commun. ***9***, 1477.

16. Zhang, B., Zhang, J., Shi, J., et al. (2019). Manganese acting as a high-performance heterogeneous electrocatalyst in carbon dioxide reduction. Nat. Commun. ***10***, 2980.

17. Chu, S., Hong, S., Masa, J., et al. (2019). Synergistic catalysis of CuO/In_2O_3 composites for highly selective electrochemical CO_2 reduction to CO. Chem. Commun. ***55***, 12380.

18. Han, Z., Changhyeok, C., Tao, H., et al. (2018). Tuning Pd-catalyzed electroreduction of CO_2 to CO with reduced overpotential. Catal. Sci. Techn. ***8***, 3894−3900.

19. Xia, C., Zhu, P., Jiang, Q., et al. (2019). Continuous production of pure liquid fuel solutions via electrocatalytic CO_2 reduction using solid-electrolyte devices. Nat. Energy ***4***, 776−785.

20. Han, N., Wang, Y., Yang, H., et al. (2018). Ultrathin bismuth nanosheets from in situ topotactic transformation for selective electrocatalytic CO_2 reduction to formate. Nat. Commun. ***9***, 1320.

21. Bushuyev, O.S., De Luna, P., Dinh, et al. (2018). What should we make with CO_2 and how can we make it. Joule ***2***, 825−832.
22. Gao, J., Zhang, H., Guo, X., et al. (2019). Selective C−C coupling in carbon dioxide electroreduction via efficient spillover of intermediates as supported by operando raman spectroscopy. J. Am. Chem. Soc. ***141***, 18704−18714.
23. Luo, M., Wang, Z., Li, Y.C., et al. (2019). Hydroxide promotes carbon dioxide electroreduction to ethanol on copper via tuning of adsorbed hydrogen. Nat. Commun. ***10***, 5814.
24. Fu, J., Zhu, W., Chen, Y., et al. (2019). Bipyridine-assisted assembly of Au nanoparticles on Cu nanowires to enhance the electrochemical reduction of CO_2. Angew. Chem. Int. Ed. ***58***, 14100−14103.
25. Kuhl, K.P., Hatsukade, T., Cave, E.R., et al. (2014). Electrocatalytic conversion of carbon dioxide to methane and methanol on transition metal surfaces. J. Am. Chem. Soc. ***136***, 14107−14113.
26. Stephanie, N., Erlend, B., Soren, B.S., et al. (2019). Progress and perspectives of electrochemical CO_2 reduction on copper in aqueous electrolyte. Chem. Rev. ***119***, 7610−7672.
27. Kuhl, K.P., Cave, E.R., Abram, D.N., et al. (2012). New insights into the electrochemical reduction of carbon dioxide on metallic copper surfaces. Energy Environ. Sci. ***5***, 7050.
28. Zhong, M., Tran, K., Min, Y., et al. (2020). Accelerated discovery of CO_2 electrocatalysts using active machine learning. Nature ***581***, 178−183.
29. Zhuang, T.-T., Liang, Z.-Q., Seifitokaldani, A., et al. (2018). Steering post C–C coupling selectivity enables high efficiency electroreduction of carbon dioxide to multi-carbon alcohols. Nat. Catal. ***1***, 421−428.
30. Wang, X., Wang, Z., Arquer, F.P.G., et al. (2020). Efficient electrically powered CO_2-to-ethanol via suppression of deoxygenation. Nat. Energy, ***5***, 478−486.
31. Pokharel, U.R., Fronczek, F.R., Maverick, A.W. (2014). Reduction of carbon dioxide to oxalate by a binuclear copper complex. Nat. Commun. ***5***, 5883.
32. Wang, H., Tzeng, Y.K., Ji, Y., et al. (2020). Synergistic enhancement of electrocatalytic CO_2 reduction to C_2 oxygenates at nitrogen-doped nanodiamonds/Cu interface. Nat. Nanotechnol. ***15***, 131−137.

33. De, R., Gonglach, S., Paul, S., et al. (2020). Electrocatalytic reduction of CO_2 to acetic acid by a molecular manganese corrole complex. Angew. Chem. Int. Ed. ***59***, 10527−10534.

34. Zhao, K., Nie, X., Wang, H., et al. (2020). Selective electroreduction of CO_2 to acetone by single copper atoms anchored on N-doped porous carbon. Nat. Commun. ***11***, 2455.

35. Rahman, D., Wibawa Hendra, S., Hassan, M., et al. (2020). A disquisition on the active sites of heterogeneous catalysts for electrochemical reduction of CO_2 to value added chemicals and fuel. Adv. Energy Mater. ***10***, 1902106.

36. Birdja, Y.Y., Pérez-Gallent, E., Figueiredo, M.C., et al. (2019). Advances and challenges in understanding the electrocatalytic conversion of carbon dioxide to fuels. Nat. Energy. ***4***, 732–745.

37. Sun, L., Reddu, V., Fisher, A.C. (2020). Electrocatalytic reduction of carbon dioxide: opportunities with heterogeneous molecular catalysts. Energy Environ. Sci. ***13***. 374–403.

38. Francke, R., Schille, B., Roemelt, M. (2018). Homogeneously catalyzed electroreduction of carbon dioxide—methods, mechanisms, and catalysts. Chem. Rev. ***118***, 4631–4701.

39. Li, M., Wang, H., Luo, W., et al. (2020). Heterogeneous Single-Atom Catalysts for Electrochemical CO_2 Reduction Reaction, Adv Mater, ***32***, e2001848.

40. Yang, J., Li, W., Wang, D., Li, Y. (2020). Electronic Metal-Support Interaction of Single-Atom Catalysts and Applications in Electrocatalysis, Adv Mater, ***32***, e2003300.

41. Qu, Q., Ji, S., Chen, Y., et al. (2021). The atomic-level regulation of single-atom site catalysts for the electrochemical CO_2 reduction reaction, Chem Sci, ***12***, 4201-4215.

42. Fan, Q., Zhang, M., Jia, M., et al. (2018). Electrochemical CO_2 reduction to C_{2+} species: Heterogeneous electrocatalysts, reaction pathways, and optimization strategies, Mater. Today Energy, ***10***, 280-301.

43. Ma, T., Fan, Q., Li, X., et al. (2019). Graphene-based materials for electrochemical CO_2 reduction. J. CO_2 Util. ***30***, 168–182.

44. Wang, Y., Han, P., Lv, X., et al. (2018). Defect and Interface Engineering for

Aqueous Electrocatalytic CO_2 Reduction, Joule, ***2***, 2551-2582.

45. Zhu, D.D., Liu, J.L., Qiao, S.Z. (2016). Recent Advances in Inorganic Heterogeneous Electrocatalysts for Reduction of Carbon Dioxide, Adv. Mater., ***28***, 3423-3452.

46. Albero, J., Peng, Y., García, H. (2020). Photocatalytic CO_2 reduction to C_{2+} products. ACS Catal. ***10***, 5734–5749.

47. Sun, Z., Ma, T., Tao, H., et al. (2017). Fundamentals and challenges of electrochemical CO_2 reduction using two-dimensional materials. Chem ***3***, 560–587.

48. Pegis, M.L., Roberts, J.A.S., Wasylenko, D.J., et al. (2015). Standard reduction potentials for oxygen and carbon dioxide couples in acetonitrile and *N*,*N*-dimethylformamide. Inorg. Chem. ***54***, 11883–11888.

49. Costentin, C., Drouet, S., Robert, M., et al. (2012). A local proton source enhances CO_2 electroreduction to CO by a molecular Fe catalyst. Science ***338***, 90–94.

50. Centi, G., Perathoner, S., Win, G., et al. (2007). Electrocatalytic conversion of CO_2 to long carbon-chain hydrocarbons. Green Chem. ***9***, 671–678.

51. Lopes, P.P., Strmcnik, D., Tripkovic, D., et al. (2016). Relationships between atomic level surface structure and stability/activity of platinum surface atoms in aqueous environments. ACS Catal. ***6***, 2536–2544.

52. Zheng, Y., Vasileff, A., Zhou, X., et al. (2019). Understanding the roadmap for electrochemical reduction of CO_2 to multi-carbon oxygenates and hydrocarbons on copper-based catalysts. J. Am. Chem. Soc. ***141***, 7646–7659.

53. Hori, Y., Takahashi, R., Yoshinami, Y., et al. (1997). Electrochemical reduction of CO at a copper electrode. J. Phys. Chem. B ***101***, 7075–7081.

54. Montoya, J.H., Shi, C., Chan, K., et al. (2015). Theoretical insights into a CO dimerization mechanism in CO_2 electroreduction. J. Phys. Chem. Lett. ***6***, 2032–2037.

55. Calle-Vallejo, F., Koper, M.T.M. (2013). Theoretical considerations on the electroreduction of CO to C_2 species on Cu(100) electrodes. Angew. Chem. Int. Ed. *52*. 7282–7285.

56. Gao, D., Arán-Ais, R.M., Jeon, H.S., et al. (2019). Rational catalyst and electrolyte design for CO_2 electroreduction towards multicarbon products. Nat.

Catal. ***2***, 198–210.
57. Garza, A.J, Bell, A.T., Head-Gordon, M. (2018). Mechanism of CO_2 reduction at copper surfaces: pathways to C_2 products. ACS Catal. ***8***, 1490–1499.
58. Zhang, H., Li, J., Cheng, M.-J. et al. (2018). CO electroreduction: current development and understanding of Cu-based catalyst. ACS Catal. ***9***, 49–65.
59. Nie, X., Esopi, M.R., Janik, M.J., et al. (2013). Selectivity of CO_2 reduction on copper electrodes: the role of the kinetics of elementary steps. Angew. Chem. Int. Ed. ***125***, 2519–2522.
60. Kuhl, K.P., Cave, E.R., Abram, D.N., et al. (2012). New insights into the electrochemical reduction of carbon dioxide on metallic copper surfaces. Energy Environ. Sci. ***5***, 7050–7059.
61. Schouten, K.J.P., Kwon, Y., van der Ham, C.J.M., et al. (2011). A new mechanism for the selectivity to C_1 and C_2 species in the electrochemical reduction of carbon dioxide on copper electrodes. Chem. Sci. ***2***, 1902–1909.
62. Cheng, T., Xiao, H., Goddard, W.A. (2017). Full atomistic reaction mechanism with kinetics for CO reduction on Cu(100) from ab initio molecular dynamics free-energy calculations at 298 K. Proc. Natl. Acad. Sci. U. S. A. ***114***, 1795–1800.
63. Alejandro J. Garza, A.T.B., Martin Head-Gordon (2018). Mechanism of CO_2 Reduction at Copper Surfaces: Pathways to C2 Products, ACS Catal., ***8***, 1490-1499.
64. Kas, R., Kortlever, R., Milbrat, A., et al. (2014). Electrochemical CO_2 reduction on Cu_2O-derived copper nanoparticles: controlling the catalytic selectivity of hydrocarbons. Phys. Chem. Chem. Phys. ***16***, 12194–12201.
65. Genovese, C., Ampelli, C., Perathoner, S., et al. (2017). Mechanism of C–C bond formation in the electrocatalytic reduction of CO_2 to acetic acid. A challenging reaction to use renewable energy with chemistry. Green Chem. ***19***, 2406–2415.
66. Sun, X., Zhu, Q., Kang, X., et al. (2017). Design of a Cu(i)/C-doped boron nitride electrocatalyst for efficient conversion of CO_2 into acetic acid. Green Chem. ***19***, 2086–2091.
67. Chen, C.S., Wan, J.H., Yeo, B.S. (2015). Electrochemical reduction of carbon dioxide to ethane using nanostructured Cu_2O-derived copper catalyst and

palladium(II) chloride. J. Phys. Chem. C ***119***, 26875–26882.

68. Li, C.W., Kanan, M.W. (2012). CO_2 reduction at low overpotential on Cu electrodes resulting from the reduction of thick Cu_2O films. J. Am. Chem. Soc. ***134***, 7231–7234.

69. Sen, S., Dan, L., Palmore, G.T.R. (2014). Electrochemical reduction of CO_2 at copper nanofoams. ACS Catal. ***4***, 3091–3095.

70. Handoko, A.D., Chan, K.W., Yeo, B.S. (2017). $–CH_3$ mediated pathway for the electroreduction of CO_2 to ethane and ethanol on thick oxide-derived copper catalysts at low overpotentials. ACS Energy Lett. ***2***, 2103–2109.

71. Zhuang, T.-T., Pang, Y., Liang, Z.-Q., et al. (2018). Copper nanocavities confine intermediates for efficient electrosynthesis of C_3 alcohol fuels from carbon monoxide, Nat. Catal. ***1***, 946–951.

72. Clark, E.L., Bell, A.T. (2018). Direct observation of the local reaction environment during the electrochemical reduction of CO_2. J. Am. Chem. Soc. ***140***, 7012–7020.

73. Gao, J., Bahmanpour, A., Krocher, O., Zakeeruddin, S.M., Ren, D., Gratzel, M. (2023). Electrochemical synthesis of propylene from carbon dioxide on copper nanocrystals, Nat Chem, ***15***, 705-713.

74. Zheng, X., Ji, Y., Tang, J., et al. (2018). Theory-guided Sn/Cu alloying for efficient CO_2 electroreduction at low overpotentials. Nat. Catal. ***2***, 55–61.

75. Yang, F., Elnabawy, A.O., Schimmenti, R., et al. (2020). Bismuthene for highly efficient carbon dioxide electroreduction reaction. Nat. Commun. ***11***, 1088.

76. Wang, Y.-R., Huang, Q., He, C.-T., et al. (2018). Oriented electron transmission in polyoxometalate-metalloporphyrin organic framework for highly selective electroreduction of CO_2. Nat. Commun. ***9***, 4466.

77. Li, J., Kuang, Y., Meng, Y., et al. (2020). Electroreduction of CO_2 to formate on a copper-based electrocatalyst at high pressures with high energy conversion efficiency. J. Am. Chem. Soc. ***142***, 7276–7282.

78. Wang, X., Xu, A., Li, F., et al. (2020). Efficient methane electrosynthesis enabled by tuning local CO_2 availability. J. Am. Chem. Soc. ***142***, 3525–3531.

79. Wang, Y., Liu, X., Han, X., et al. (2020). Unique hole-accepting carbon-dots promoting selective carbon dioxide reduction nearly 100% to methanol by pure

water. Nat. Commun. ***11***, 2531.

80. Wu, Y., Jiang, Z., Lu, X., et al. (2019). Domino electroreduction of CO_2 to methanol on a molecular catalyst. Nature ***575***, 639–642.

81. Wang, Y., Wang, Z., Dinh, C.-T., et al. (2019). Catalyst synthesis under CO_2 electroreduction favours faceting and promotes renewable fuels electrosynthesis. Nat. Catal. ***3***, 98–106.

82. Li, F., Thevenon, A., Rosas-Hernández, A., et al. (2019). Molecular tuning of CO_2-to-ethylene conversion. Nature ***577***, 509–513.

83. Vasileff, A., Zhu, Y., Zhi, X., et al. (2020). Electrochemical reduction of CO_2 to ethane through stabilization of an ethoxy intermediate. Angew. Chem. Int. Ed. ***132***, 19817–196821.

84. Kibria, M.G., Dinh, C.T., Seifitokaldani, A., et al. (2018). A Surface Reconstruction Route to High Productivity and Selectivity in CO_2 Electroreduction toward C_{2+} Hydrocarbons, Adv Mater, ***30***, e1804867.

85. Padilla, M., Baturina, O., Gordon, J.P., et al. (2017). Selective CO_2 electroreduction to C_2H_4 on porous Cu films synthesized by sacrificial support method. J. CO_2 Util. ***19***, 137–145.

86. Luna, P.D., Quintero-Bermudez, R., Dinh, C.-T., et al. (2018). Catalyst electro-redeposition controls morphology and oxidation state for selective carbon dioxide reduction. Nat. Catal. ***1***, 103–110.

87. Mistry, H., Varela, A.S., Bonifacio, C.S., et al. (2016). Highly selective plasma-activated copper catalysts for carbon dioxide reduction to ethylene. Nat. Commun. ***7***, 12123.

88. Lee, S.Y., Jung, H., Kim, N.-K., et al. (2018). Mixed copper states in anodized Cu electrocatalyst for stable and selective ethylene production from CO_2 reduction. J. Am. Chem. Soc. ***140***, 8681–8689.

89. Chen, C.S., Handoko, A.D., Wan, J.H., et al. (2015). Stable and selective electrochemical reduction of carbon dioxide to ethylene on copper mesocrystals. Catal. Sci. Technol. ***5***, 161–168.

90. Baturina, O., Lu, Q., Xu, F., et al. (2016). Effect of nanostructured carbon support on copper electrocatalytic activity toward CO_2 electroreduction to hydrocarbon fuels. Catal. Today ***288***, 2–10.

91. Gu, Z., Yang, N., Han, P., Kuang, M., Zheng, G. (2019). Oxygen vacancy

tuning toward efficient electrocatalytic CO_2 reduction to C_2H_4, Small method, ***3***, 1800449.

92. Wan, Q., Zhang, J., Zhang, B., et al. (2020). Boron-doped CuO nanobundles for electroreduction of carbon dioxide to ethylene. Green Chem. ***22***, 2750–2754.

93. Kim, J., Choi, W., Park, J.W., et al. (2019). Branched copper oxide nanoparticles induce highly selective ethylene production by electrochemical carbon dioxide reduction. J. Am. Chem. Soc. ***141***, 6986–6994.

94. Duan, Y.X., Meng, F.L., Liu, K.H., et al. (2018). Amorphizing of Cu nanoparticles toward highly efficient and robust electrocatalyst for CO_2 reduction to liquid fuels with high faradaic efficiencies. Adv. Mater. ***30***, 17061941–17061947.

95. Zhao, K., Liu, Y., Quan, X., et al. (2017). CO_2 electroreduction at low overpotential on oxide-derived Cu/carbons fabricated from metal organic framework. ACS Appl. Mater. Interfaces ***9***, 5302–5311.

96. Jiao, Y., Zheng, Y., Chen, P., et al. (2017). Molecular scaffolding strategy with synergistic active centers to facilitate electrocatalytic CO_2 reduction to hydrocarbon/alcohol. J. Am. Chem. Soc. ***139***, 18093–18100.

97. Su, X., Sun, Y., Jin, L., et al. (2020). Hierarchically porous Cu/Zn bimetallic catalysts for highly selective CO_2 electroreduction to liquid C_2 products. Appl. Catal. B Environ. ***269***, 118800.

98. Ren, D., Ang, B.S.-H., Yeo, B.S. (2016). Tuning the selectivity of carbon dioxide electroreduction toward ethanol on oxide-derived Cu_xZn catalysts. ACS Catal. ***6***, 8239–8247.

99. Wang, H., Matios, E., Wang, C., et al. (2019). Rapid and scalable synthesis of cuprous halide-derived copper nano-architectures for selective electrochemical reduction of carbon dioxide, Nano Lett. ***19***, 3925–3932.

100. Ren, D., Wong, N.T., Handoko, A.D., et al. (2016). Mechanistic insights into the enhanced activity and stability of agglomerated Cu nanocrystals for the electrochemical reduction of carbon dioxide to n-propanol. J. Phys. Chem. Lett. *7*, 20-24.

101. Wu, M., Zhu, C., Wang, K., et al. (2020). Promotion of CO_2 electrochemical reduction via Cu nanodendrites. ACS Appl. Mater. Interfaces ***12***, 11562–11569.

102. Yang, K.D., Ko, W.R., Lee, J.H., et al. (2016). Morphology-directed selective production of ethylene or ethane from CO_2 on a Cu mesopore electrode. Angew. Chem. Int. Ed. ***56***, 796–800.

103. Ren, D., Deng, Y., Handoko, A.D., et al. (2015). Selective electrochemical reduction of carbon dioxide to ethylene and ethanol on copper(I) oxide catalysts. ACS Catal. ***5***, 2814–2821.

104. Arán-Ais, R.M., Scholten, F., Kunze, S., et al. (2020). The role of in situ generated morphological motifs and Cu(i) species in C_{2+} product selectivity during CO_2 pulsed electroreduction. Nat. Energy ***5***, 317–325.

105. Ma, M., Djanashvili, K., Smith, W.A. (2016). Controllable hydrocarbon formation from the electrochemical reduction of CO_2 over Cu nanowire arrays. Angew. Chem. Int. Ed. ***55***, 6680–6684.

106. Gao, D., Zegkinoglou, I., J. Divins, N., et al. (2017). Plasma-activated copper nanocube catalysts for efficient carbon dioxide electroreduction to hydrocarbons and alcohols. ACS Nano ***11***, 4825–4831.

107. Hori, Y., Takahashi, I., Koga, O., et al. (2003). Electrochemical reduction of carbon dioxide at various series of copper single crystal electrodes. J. Mol. Catal. A Chem. ***199***, 39–47.

108. Hoko, A.D., Ong, C.W., Huang, Y., et al. (2016). Mechanistic insights into the selective electroreduction of carbon dioxide to ethylene on Cu_2O-derived copper catalysts. J. Phys. Chem. C ***120***, 20058–20067.

109. Liang, Z.-Q., Zhuang, T.-T., Seifitokaldani, A., et al. (2018). Copper-on-nitride enhances the stable electrosynthesis of multi-carbon products from CO_2. Nat. Commun. ***9***, 3828.

110. Ishimaru, S., Shiratsuchi, R., Nogami, G. (2000). Pulsed electroreduction of CO_2 on Cu-Ag alloy electrodes. J. Electrochem. Soc. ***147***, 1864–1867.

111. Ke, F.S., Liu, X.C., Wu, J., et al. (2016). Selective formation of C_2 products from the electrochemical conversion of CO_2 on CuO-derived copper electrodes comprised of nanoporous ribbon arrays. Catal. Today ***288***, 18–23.

112. Kim, D., Kley, C.S., Li, Y., et al. (2017). Copper nanoparticle ensembles for selective electroreduction of CO_2 to C_2-C_3 products. Proc. Natl. Acad. Sci. U. S. A. ***114***, 10560–10565.

113. Hahn, C., Hatsukade, T., Kim, Y.G., et al. (2017). Engineering Cu

surfaces for the electrocatalytic conversion of CO_2: controlling selectivity toward oxygenates and hydrocarbons. Proc. Natl. Acad. Sci. U. S. A. ***114***, 5918–5923.

114. Jeon, H.S., Kunze, S., Scholten, F., et al. (2017). Prism-shaped Cu nanocatalysts for electrochemical CO_2 reduction to ethylene. ACS Catal. ***8***, 531–535.

115. Qiu, X.F., Zhu, H.L., Huang, J.R., et al. (2021). Highly selective CO_2 electroreduction to C_2H_4 using a metal-organic framework with dual active sites. J. Am. Chem. Soc. ***143***, 7242−7246.

116. Yuan, X., Chen, S., Cheng, D., et al. (2021). Controllable Cu(0)-Cu(+) Sites for electrocatalytic reduction of carbon dioxide. Angew. Chem. Int. Ed. ***60***, 15344–15347.

117. Pranit Iyengar, M.J.K., James R. Pankhurst, Federico C.V., et al. (2021). Elucidating the Facet-Dependent Selectivity for CO_2 Electroreduction to Ethanol of Cu−Ag Tandem Catalysts, ACS Catal. ***11***, 4456−4463.

118. Kim, T., Palmore, G. T. R. (2020). A scalable method for preparing Cu electrocatalysts that convert CO_2 into C_{2+} products. Nat. Commun. ***11,*** 3622.

119. Peng, C., Luo, G., Zhang, J., et al. (2021). Double sulfur vacancies by lithium tuning enhance CO_2 electroreduction to n-propanol. Nat. Commun. ***12***, 1580.

120. Qiu, X.F., Zhu, H.L., Huang, J.R., et al. (2021). Highly selective CO_2 electroreduction to C_2H_4 using a metal-organic framework with dual active sites. J. Am. Chem. Soc. ***143***, 7242−7246.

121. Han, H., Noh, Y., Kim, Y., et al. (2020). Selective electrochemical CO_2 conversion to multicarbon alcohols on highly efficient N-doped porous carbon-supported Cu catalysts. Green Chem. ***22***, 71–84.

122. Jiang, K., Sandberg, R.B., Akey, A.J., et al. (2018). Metal ion cycling of Cu foil for selective C–C coupling in electrochemical CO_2 reduction. Nat. Catal. ***1***, 111–119.

123. Li, Q., Zhu, W., Fu, J., et al. (2016). Controlled assembly of Cu nanoparticles on pyridinic-N rich graphene for electrochemical reduction of CO_2 to ethylene. Nano Energy ***24***, 1–9.

124. Rahaman, M., Dutta, A., Zanetti, A., et al. (2017). Electrochemical reduction of CO_2 into multicarbon alcohols on activated Cu mesh catalysts: an

identical location (IL) study. ACS Catal. *7*, 7946–7956.

125. Liang, H., Hu, X., Ceccato, M., et al. (2021). Hydrophobic copper interfaces boost electroreduction of carbon dioxide to ethylene in water. ACS Catal. ***11***, 958−966.

126. Albo, J., Vallejo, D., Beobide, G., et al. (2017). Copper-Based Metal-Organic Porous Materials for CO_2 Electrocatalytic Reduction to Alcohols, ChemSusChem, ***10***, 1100-1109.

127. Wang, H., Tzeng, Y.K., Ji, Y., et al. (2020). Synergistic enhancement of electrocatalytic CO_2 reduction to C_2 oxygenates at nitrogen-doped nanodiamonds/Cu interface, Nat Nanotechnol, ***15***, 131-137.

128. Zhang, W., Huang, C., Xiao, Q., et al. (2020). Atypical oxygen-bearing copper boosts ethylene selectivity toward electrocatalytic CO_2 reduction. J. Am. Chem. Soc. ***142***, 11417–11427.

129. Monzó, J., Malewski, Y., Kortlever, R., et al. (2015). Enhanced electrocatalytic activity of Au@Cu core@shell nanoparticles towards CO_2 reduction, J. Mater. Chem. A ***3***, 23690–23698.

130. Li, F., Thevenon, A., Rosas-Hernandez, A., et al. (2020). Molecular tuning of CO_2-to-ethylene conversion. Nature, ***577***, 509–513.

131. Wakerley, D., Lamaison, S., Ozanam, F., et al. (2019) Bio-inspired hydrophobicity promotes CO_2 reduction on a Cu surface. Nat Mater, ***18***, 1222-1227.

132. Lum, Y., Yue, B., Lobaccaro, P., et al. (2017). Optimizing C–C coupling on oxide-derived copper catalysts for electrochemical CO_2 reduction. J. Phys. Chem. C ***121***, 14191–14203.

133. Zhang, F.Y., Sheng, T., Tian, N., et al. (2017). Cu overlayers on tetrahexahedral Pd nanocrystals with high-index facets for CO_2 electroreduction to alcohols, Chem. Commun. ***53***, 8085–8088.

134. Geioushy, R.A., Khaled, M.M., Alhooshani, K., et al. (2017). Graphene/ZnO/Cu_2O electrocatalyst for selective conversion of CO_2 into n-propanol. Electrochim. Acta ***245***, 456–462.

135. Dutta, A., Rahaman, M., Mohos, M., et al. (2017). Electrochemical CO_2 conversion using skeleton (sponge) type of Cu catalysts. ACS Catal. *7*, 5431–5437.

136. Dutta, A., Rahaman, M., Luedi, N.C., et al. (2016). Morphology matters: tuning the product distribution of CO_2 electroreduction on oxide-derived Cu foam catalysts. ACS Catal. ***6***, 3804–3814.

137. Geioushy, R.A., Khaled, M.M., Hakeem, A.S., et al. (2017). High efficiency graphene/Cu_2O electrode for the electrochemical reduction of carbon dioxide to ethanol, J. Electroanal. Chem. ***785***, 138–143.

138. Wang, Z., Yang, G., Zhang, Z., et al. (2016). Selectivity on etching: creation of high-energy facets on copper nanocrystals for CO_2 electrochemical reduction. ACS Nano ***10***, 4559–4564.

139. Chi, D., Yang, H., Du, Y., et al. (2014). Morphology-controlled CuO nanoparticles for electroreduction of CO2 to ethanol, RSC Adv. ***4***, 37329–37332.

140. Yuan, J., Liu, L., Guo, R., et al. (2017). Electroreduction of CO_2 into ethanol over an active catalyst: copper supported on titania. Catalysts *7*, 220.

141. Reller, C., Krause, R., Volkova, E., et al. (2017). Selective electroreduction of CO_2 toward ethylene on nano dendritic copper catalysts at high current density. Adv. Energy Mater. *7*, 1602114.1–1602114.8.

142. Zhou, Y., Che, F., Liu, M., et al. (2018). Dopant-induced electron localization drives CO_2 reduction to C_2 hydrocarbons, Nat Chem, ***10***, 974-980.

143. Lee, S., Park, G., Lee, J. (2017). Importance of Ag–Cu biphasic boundaries for selective electrochemical reduction of CO_2 to ethanol. ACS Catal. *7*, 8594–8604.

144. Kusama, S., Saito, T., Hashiba, H., et al. (2017). Crystalline copper(II) phthalocyanine catalysts for electrochemical reduction of carbon dioxide in aqueous media, ACS Catal. *7*, 8382–8385.

145. Jiwanti, P.K., Natsui, K., Nakata, K., et al. (2018). The electrochemical production of C_2/C_3 species from carbon dioxide on copper-modified boron-doped diamond electrodes. Electrochim. Acta, ***266***, 414–419.

146. Martić, N., Reller, C., Macauley, C., et al. (2019). Paramelaconite-enriched copper-based material as an efficient and robust catalyst for electrochemical carbon dioxide reduction. Adv. Energy Mater. ***9***, 1901228.

147. Ma, W., Xie, S., Liu, T., et al. (2020). Electrocatalytic reduction of CO_2 to ethylene and ethanol through hydrogen-assisted C–C coupling over fluorine-modified copper. Nat. Catal. ***3***, 478–487

148. Hoang, T.T.H., Ma, S., Gold, J.I., et al. (2017). Nanoporous copper films by additive-controlled electrodeposition: CO_2 reduction catalysis. ACS Catal. ***7***, 3313–3321.

149. Ma, S., Sadakiyo, M., Luo, R., et al. (2016). One-step electrosynthesis of ethylene and ethanol from CO_2 in an alkaline electrolyzer. J. Power Sources ***301***, 219–228.

150. De Gregorio, G.L., Burdyny, T., Loiudice, A., et al. (2020). Facet-dependent selectivity of Cu catalysts in electrochemical CO_2 reduction at commercially viable current densities, ACS Catal. ***10***, 4854-4862.

151. Lv, J.-J., Jouny, M., Luc, W., et al. (2018). A highly porous copper electrocatalyst for carbon dioxide reduction. Adv. Mater. ***30***, 1803111.1-1803111.8.

152. Thao T. H. Hoang, S.V., Sichao Ma, et al. (2018). Nano porous copper-silver alloys by additive-controlled electro-deposition for the selective electroreduction of CO_2 to ethylene and ethanol. J. Am. Chem. Soc. ***140***, 5791–5797.

153. Ma, S., Sadakiyo, M., Heima, M., et al. (2017). Electroreduction of Carbon Dioxide to Hydrocarbons Using Bimetallic Cu-Pd Catalysts with Different Mixing Patterns, J. Am. Chem. Soc. ***139***, 47–50.

154. Chen, X., Henckel, D.A., Nwabara, U.O., et al. (2019). Controlling speciation during CO_2 reduction on Cu-alloy electrodes. ACS Catal. ***10***, 672–682.

155. Yang, P.P., Zhang, X.L., Gao, F.Y., et al. (2020). Protecting Copper Oxidation State via Intermediate Confinement for Selective CO_2 Electroreduction to C_{2+} Fuels, J. Am. Chem. Soc. ***142***, 6400–6408.

156. Dinh, C.-T., Burdyny, T., Kibria, M.G., et al. (2018). CO_2 electroreduction to ethylene via hydroxide-mediated copper catalysis at an abrupt interface. Science ***360***, 783–787.

157. Pan, F., Yang, Y. (2020). Designing CO_2 reduction electrode materials by morphology and interface engineering. Energy Environ. Sci. ***13***, 2275−2309.

158. Shi, Y., Lyu, Z., Zhao, M., et al. (2021). Noble-metal nanocrystals with controlled shapes for catalytic and electrocatalytic applications. Chem. Rev. ***121***, 649−735.

159. Yin, J., Wang, J., Ma, Y., et al. (2020). Recent advances in the controlled

synthesis and catalytic applications of two-dimensional rhodium nanomaterials, ACS Mater. Lett. ***3***, 121−133.

160. Wang, Y., Liu, H., Yu, J., Hu, B., Zhao, H., Tsiakaras, P., Song, S. (2019) Copper oxide derived nanostructured self-supporting Cu electrodes for electrochemical reduction of carbon dioxide, Electrochimica Acta, ***328***, 135083.

161. Lei, F., Liu, W., Sun, Y., et al. (2016). Metallic tin quantum sheets confined in graphene toward high-efficiency carbon dioxide electroreduction. Nat. Commun. *7*, 12697.

162. An, B., Zhang, J., Cheng, K., et al. (2017). Confinement of ultrasmall Cu/ZnO_x nanoparticles in metal-organic frameworks for selective methanol synthesis from catalytic hydrogenation of CO_2. J. Am. Chem. Soc. ***139***, 3834−3840

163. Shifa, T.A., Vomiero, A. (2019). Confined catalysis: progress and prospects in energy conversion. Adv. Energy Mater. ***9***, 1902307.

164. Petrosko, S.H., Johnson, R., White, H., et al. (2016). Nanoreactors: small spaces, big implications in chemistry. J. Am. Chem. Soc. ***138***, 7443−7445.

165. Knossalla, J., Paciok, P., Gohl, D., et al. (2018). Shape-controlled nanoparticles in pore-confined space. J. Am. Chem. Soc. ***140***, 15684−15689.

166. O'Mara, P.B., Wilde, P., Benedetti, T.M., et al. (2019). Cascade reactions in nanozymes: spatially separated active sites inside Ag-core-porous-Cu-shell nanoparticles for multistep carbon dioxide reduction to higher organic molecules. J. Am. Chem. Soc. ***141***, 14093−14097.

167. Yun, H., Handoko, A.D., Hirunsit, P., et al. (2017). Electrochemical reduction of CO_2 using copper single-crystal surfaces: effects of CO* coverage on the selective formation of ethylene. ACS Catal. *7*, 1749−1756.

168. Gao, Y., Wu, Q., Liang, X., et al. (2020). Cu_2O nanoparticles with both {100} and {111} facets for enhancing the selectivity and activity of CO_2 electroreduction to ethylene. Adv. Sci. *7*, 1902820.

169. Chu, S., Yan, X., Choi, C., et al. (2020). Stabilization of Cu^+ by tuning a $CuO–CeO_2$ interface for selective electrochemical CO_2 reduction to ethylene. Green Chem. ***22***, 6540−6546.

170. Li, X., Li, L., Xia, Q., et al. (2022). Selective electroreduction of CO_2 and CO to C_2H_4 by synergistically tuning nanocavities and the surface charge of

copper oxide. ACS Sustain. Chem. Eng. ***10***, 6466−6475.

171. Wang, D., Li, L., Xia, Q., et al. (2022). Boosting CO_2 electroreduction to multicarbon products via tuning of the copper surface charge. ACS Sustain. Chem. Eng. ***10***, 11451−11458.

172. Peterson, A.A., Abild-Pedersen, F., Studt, Felix., et al. (2010). How copper catalyzes the electroreduction of carbon dioxide into hydrocarbon fuels. Energy Environ. Sci. ***3***, 1311−1315.

173. Garza, A.J., Bell, A.T., Head-Gordon, M. (2018). Is subsurface oxygen necessary for the electrochemical reduction of CO_2 on copper. J. Phys. Chem. Lett. ***9***, 601−606.

174. Shah, A.H., Wang, Y., Hussain, S., et al. (2020). New aspects of C_2 selectivity in electrochemical CO_2 reduction over oxide-derived copper. Phys. Chem. Chem. Phys. ***22***, 2046−2053.

175. Favaro, M., Xiao, H., Cheng, T., et al. (2017). Subsurface oxide plays a critical role in CO_2 activation by Cu(111) surfaces to form chemisorbed CO_2, the first step in reduction of CO_2. Proc. Natl. Acad. Sci. U. S. A. ***114***, 6706−6711.

176. Han, Z., Choi, C., Hong, S., et al. (2019). Activated TiO_2 with tuned vacancy for efficient electrochemical nitrogen reduction. Appl. Catal. B Environ. ***257***, 117896.

177. Wang, G., Ling, Y., Wang, H., et al. (2012). Hydrogen-treated WO_3 nanoflakes show enhanced photostability. Energy Environ. Sci. ***5***, 6180−6187.

178. Fang, G., Zhu, C., Chen, M., et al. (2019). Suppressing manganese dissolution in potassium manganate with rich oxygen defects engaged high-energy-density and durable aqueous zinc-ion battery. Adv. Funct. Mater. ***29***, 18083751−18083759.

179. Ye, L., Zhang, M., Huang, P., et al. (2017). Enhancing CO_2 electrolysis through synergistic control of non-stoichiometry and doping to tune cathode surface structures. Nat. Commun. ***8***, 14785.

180. Zhou, H., Zhao, Y., Xu, J., et al. (2020). Recover the activity of sintered supported catalysts by nitrogen-doped carbon atomization. Nat. Commun. ***11***, 335.

181. Ding, X., Peng, F., Zhou, J., et al. (2019). Defect engineered bioactive transition metals dichalcogenides quantum dots. Nat. Commun. ***10***, 41.

182. Jia, Y., Zhang, L., Zhuang, L., et al. (2019). Identification of active sites for acidic oxygen reduction on carbon catalysts with and without nitrogen doping. Nat. Catal. ***2***, 688−695.

183. Lu, J., Lei, Y., Lau, K.C., et al. (2013). A nanostructured cathode architecture for low charge overpotential in lithium-oxygen batteries. Nat. Commun. ***4***, 2383.

184. Xue, L., Li, Y., Liu, X., et al. (2018). Zigzag carbon as efficient and stable oxygen reduction electrocatalyst for proton exchange membrane fuel cells. Nat. Commun. ***9***, 3819.

185. Wan, S., Qi, J., Zhang, W., et al. (2017). Hierarchical Co(OH)F superstructure built by low-dimensional substructures for electrocatalytic water oxidation. Adv. Mater. ***29***, 1700286.1−1700286.10.

186. Dai, L., Xue, Y., Qu, L., et al. (2015). Metal-free catalysts for oxygen reduction reaction. Chem. Rev. ***115***, 4823−4892.

187. Duan, X., Xu, J., Wei, Z., et al. (2017). Metal-free carbon materials for CO electrochemical reduction. Adv. Mater. ***29***, 1701784.

188. Bell, D., Rall, D., Großeheide, M., et al. (2020). Tubular hollow fibre electrodes for CO_2 reduction made from copper aluminum alloy with drastically increased intrinsic porosity. Electrochem. Commun. ***111***, 106645.

189. Tao, H., Sun, X., Back, S., et al. (2017). Doping palladium with tellurium for highly selective electrocatalytic reduction of aqueous CO_2 to CO. Chem. Sci. ***9***, 483–487.

190. Sun, Y.N., Zhang, M.L., Zhao, L., et al. (2019). A N, P dual-doped carbon with high porosity as an advanced metal-free oxygen reduction catalyst. Adv. Mater. Interfaces ***6***, 1900592.

191. Wang, Q., Lei, Y., Wang, D., et al. (2019). Defect engineering in earth-abundant electrocatalysts for CO_2 and N_2 reduction. Energy Environ. Sci. ***12***, 1730−1750.

192. Zhou, Y., Che, F., Liu, M., et al. (2018). Dopant-induced electron localization drives CO_2 reduction to C_2 hydrocarbons. Nat. Chem. ***10,*** 974−980.

193. Kim, D., Resasco, J., Yu, Y., Asiri, A.M., Yang, P. (2014) Synergistic geometric and electronic effects for electrochemical reduction of carbon dioxide using gold–copper bimetallic nanoparticles, Nat. Commun., *5*, 4948.

194. Kim, D., Xie, C., Becknell, N., et al. (2017). Electrochemical Activation of CO_2 through Atomic Ordering Transformations of AuCu Nanoparticles, J. Am. Chem. Soc., ***139***, 8329-8336.

195. Zhang, S., Kang, P., Bakir, M., et al. (2015). Polymer-supported CuPd nanoalloy as a synergistic catalyst for electrocatalytic reduction of carbon dioxide to methane. Proc. Natl. Acad. Sci. U. S. A. ***112***, 15809−15814.

196. Wakerley, D., Lamaison, S., Ozanam, F., et al. (2019). Bio-inspired hydrophobicity promotes CO_2 reduction on a Cu surface, Nat. Mater. ***18***, 1222–1227.

197. Huang, W., Ma, X.Y., Wang, H., et al. (2017). Promoting effect of $Ni(OH)_2$ on palladium nanocrystals leads to greatly improved operation durability for electrocatalytic ethanol oxidation in alkaline solution. Adv. Mater. ***29***, 1703057.

198. Wang, Y., Chen, L., Yu, X., et al. (2017). Superb Alkaline Hydrogen Evolution and Simultaneous Electricity Generation by Pt-Decorated Ni_3N Nanosheets, Advanced Energy Materials, *7*, 1601390.

199. Xiao, H., Cheng, T., Goddard, W.A., et al. (2017). Atomistic Mechanisms Underlying Selectivities in C_1 and C_2 Products from Electrochemical Reduction of CO on Cu(111), J Am Chem Soc, *139*, 130-136.

200. Lee, C.W., Shin, S.-J., Jung, H., et al. (2019). Metal–oxide interfaces for selective electrochemical C–C coupling reactions. ACS Energy Lett. ***4***, 2241−2248.

201. Bai, X., Li, Q., Shi, L., et al. (2020). Hybrid Cu^0 and Cu^{x+} as atomic interfaces promote high-selectivity conversion of CO_2 to C_2H_5OH at low potential. Small ***16***, 1901981.

202. Wang, P., Qiao, M., Shao, Q., et al. (2018). Phase and structure engineering of copper tin heterostructures for efficient electrochemical carbon dioxide reduction. Nat. Commun. ***9***, 4933.

203. Liu, X., Schlexer, P., Xiao, J., et al. (2019). PH effects on the electrochemical reduction of $CO_{(2)}$ towards C_2 products on stepped copper, Nat Commun, ***10***, 32.

204. Ringe, S., Clark, E.L., Resasco, J., et al. (2019). Understanding cation effects in electrochemical CO_2 reduction, Energy Environ. Sci. ***12***, 3001−3014.

205. Akira, M., Yoshio, H. (1991). Product selectivity affected by cationic species in electrochemical reduction of CO_2 and CO at a Cu electrode. Bull. Chem. Soc. Jpn. ***64***, 123−127.

206. Frumkin, A.N. (1959). Influence of cation adsorption on the kinetics of electrode processes. Transac. Faraday Soc. ***55***, 156.

207. Mills, J.N., McCrum, I.T., Janik, M.J. (2014). Alkali cation specific adsorption onto fcc(111) transition metal electrodes. Phys. Chem. Chem. Phys. ***16***, 13699−13707.

208. Huang, J.E., Li, F.W., Ozden, A., et al. (2021). CO_2 electrolysis to multicarbon products in strong acid. Science ***372***, 1074−1078.

209. Hori, Y., Murata, A., Takahashi, R., et al. (1988). Enhanced formation of ethylene and alcohols at ambient temperature and pressure in electrochemical reduction of carbon dioxide at a copper electrode. J. Chem. Soc., Chem. Commun. 17−19.

210. Li, W., Li, L., Xia, Q., et al. (2022). Lowering C−C coupling barriers for efficient electrochemical CO_2 reduction to C_2H_4 by jointly engineering single Bi atoms and oxygen vacancies on CuO, Appl. Catal. B ***318***, 121823.

211. Gennaro, A., Isse, A.A., Severin, M.-G., et al. (1996). Mechanism of the electrochemical reduction of carbon dioxide at inert electrodes in media of low proton availability. J. Chem. Soc., Faraday Trans. ***92***, 3963−3968.

212. Cheng, Y., Hou, P., Pan, H., et al. (2020). Selective electrocatalytic reduction of carbon dioxide to oxalate by lead tin oxides with low overpotential. Appl. Catal. B Environ. ***272***, 118954.

213. Rudolph, M., Dautz, S., Jäger, E.-G. (2000). Macrocyclic [N_4^{2-}] coordinated nickel complexes as catalysts for the formation of oxalate by electrochemical reduction of carbon dioxide. J. Am. Chem. Soc. ***122***, 10821−10830.

214. Jiang, C., Zeng, S., Ma, X., et al. (2022). Aprotic phosphonium-based ionic liquid as electrolyte for high CO_2 electroreduction to oxalate. AIChE J. ***69***, e17859.

215. Fortunati, A., Risplendi, F., Re Fiorentin, M., et al. (2023). Understanding the role of imidazolium-based ionic liquids in the electrochemical

CO_2 reduction reaction. Commun Chem, ***6***, 84.

216. Lau, G.P., Schreier, M., Vasilyev, D., et al. (2016). New Insights Into the Role of Imidazolium-Based Promoters for the Electroreduction of CO_2 on a Silver Electrode, J. Am. Chem. Soc., *138*, 7820-3.

217. Liu, B., Guo, W., Gebbie, M.A. (2022). Tuning Ionic Screening To Accelerate Electrochemical CO_2 Reduction in Ionic Liquid Electrolytes, ACS Catal., *12*, 9706-9716.

218. Wang, X., de Araujo, J.F., Ju, W., et al. (2019). Mechanistic reaction pathways of enhanced ethylene yields during electroreduction of CO_2-CO co-feeds on Cu and Cu-tandem electrocatalysts. Nat. Nanotechnol. ***14***, 1063−1070.

219. Luc, W., Ko, B.H., Kattel, S., et al. (2019). SO_2-induced selectivity change in CO_2 electroreduction. J. Am. Chem. Soc. ***141***, 9902−9909.

220. Melchaeva, O., Voyame, P., Bassetto, V.C., et al. (2017). Electrochemical reduction of protic supercritical CO_2 on copper electrodes. ChemSusChem ***10***, 3660−3670.

221. Lei, Q., Zhu, H., Song, K., et al. (2020). Investigating the origin of enhanced C_{2+} selectivity in oxide-/hydroxide-derived copper electrodes during CO_2 electroreduction. J. Am. Chem. Soc. ***142***, 4213−4222.

222. Xiao, H., Goddard, W.A., Cheng, T., et al. (2017). Cu metal embedded in oxidized matrix catalyst to promote CO_2 activation and CO dimerization for electrochemical reduction of CO_2. Proc. Natl. Acad. Sci. U. S. A. ***114***, 6685−6688.

223. Wakerley, D., Lamaison, S., Ozanam, F., et al. (2019). Bio-inspired hydrophobicity promotes CO_2 reduction on a Cu surface. Nat. Mater. ***18***, 1222–1227.

224. Yang, P.P., Zhang, X.L., Gao, F.Y., et al. (2020). Protecting copper oxidation state via intermediate confinement for selective CO_2 electroreduction to C_{2+} fuels. J. Am. Chem. Soc. ***142***, 6400–6408.

225. Nitopi, S., Bertheussen, E., Scott, S.B., et al. (2019). Progress and Perspectives of Electrochemical CO_2 Reduction on Copper in Aqueous Electrolyte, Chem Rev., ***119***, 7610-7672.

226. Li, Y., Cui, F., Ross, M.B., et al. (2017). Structure-sensitive CO_2 electroreduction to hydrocarbons on ultrathin 5-fold twinned copper nanowires. Nano Lett. ***17***, 1312−1317.

227. Zhang, L., Wei, Z., Thanneeru, S., et al. (2019). A polymer solution to prevent nanoclustering and improve the selectivity of metal nanoparticles for electrocatalytic CO_2 reduction. Angew. Chem. Int. Ed. ***58***, 15834−15840.
228. Guntern, Y.T., Pankhurst, J.R., Vavra, J., et al. (2019). Nanocrystal/metal-organic framework hybrids as electrocatalytic platforms for CO_2 conversion. Angew. Chem. Int. Ed. ***58***, 12632−12639.
229. Xu, L., Ma, X., Wu, L., et al. (2022). In situ periodic regeneration of catalyst during CO_2 electroreduction to C_{2+} products. Angew. Chem. Int. Ed. ***61***, e202210375.